LAWRENCE
LIVERMORE
NATIONAL
LABORATORY

LLNL-JRNL-472631

Land subsidence in the Cerro Prieto Geothermal Field, 1 Baja California, Mexico, from 1994 to 2005. An integrated analysis of DInSAR, levelingand geological data.

O. Sarychikhina, E. Glowacka, R. Mellors, F. S. Vidal

March 9, 2011

Journal of Volcanology and Geothermal Research

Disclaimer

Land subsidence in the Cerro Prieto Geothermal Field, Baja California, Mexico, from 1994 to 2005. An integrated analysis of DInSAR, leveling and geological data.

Olga Sarychikhina[1,*], Ewa Glowacka[1], Robert Mellors[2], Francisco Suárez Vidal[1]

[1] División de Ciencias de la Tierra, CICESE, Carretera Ensenada-Tijuana # 3918, Zona Playitas, Ensenada, Baja California, México, C. P. 22860.

[2] Department of Geological Sciences, San Diego State University, 5500 Campanile Drive, San Diego, CA 92182, USA.

*Corresponding author. Tel.: +52 (646) 1750500 Ext. 26564; fax: +52 (646)1750559
E-mail address: osarycth@cicese.mx (O. Sarychikhina)

Abstract

Cerro Prieto is the oldest and largest Mexican geothermal field in operation and has been producing electricity since 1973. The large amount of geothermal fluids extracted to supply steam to the power plants has resulted in considerable deformation in and around the field. The deformation includes land subsidence and related ground fissuring and faulting. These phenomena have produced severe damages to infrastructure such as roads, irrigation canals and other facilities.

In this paper, the technique of Differential Synthetic Aperture Radar Interferometry (DInSAR) is applied using C-band ENVISAR ASAR data acquired between 2003 and 2006 to determine the extent and amount of land subsidence in the Mexicali Valley near Cerro Prieto Geothermal Field. The DInSAR results were compared with published data from precise leveling surveys (1994-1997 and 1997-2006) and detailed geological information in order to improve the understanding of temporal and spatial distributions of anthropogenic subsidence in the Mexicali Valley. The leveling and DInSAR data were modeled to characterize the observed deformation in terms of fluid extraction.

The results confirm that the tectonic faults control the spatial extent of the observed subsidence. These faults likely act as groundwater flow barriers for aquifers and reservoirs. The shape of the

subsiding area coincides with the Cerro Prieto pull-apart basin. In addition, the spatial pattern of the subsidence as well as changes in rate are highly correlated with the development of the Cerro Prieto Geothermal Field.

Keywords: Cerro Prieto Geothermal Field, geothermal fluids extraction, land subsidence, DInSAR, leveling surveys, geological data.

Research Highlights

Exploitation of the Cerro Prieto Geothermal field causes ground deformation in the Mexicali Valley. → Integrated analysis of satellite observations, ground-based geological and geodetic measurements was performed. → Modeling of observed deformation was conducted. → The changes in subsidence spatial pattern and rate are highly correlated with the development of the CPGF. → The spatial extent of the observed subsidence is controlled by tectonic faults.

1. Introduction

Extraction of fluids from geothermal systems at a rate higher than the natural recharge and/or man-made injection may result in land subsidence due to the lowering of pressure in the reservoir and surrounding rocks. Surface deformation occurs even if the reservoir is deep and isolated from shallow groundwater (Vasco *et al.*, 2002). Land subsidence rates of up to dozens of centimeters per year have been measured across several major geothermal fields (e.g., Geysers, USA (Mossop and Segall, 1997), Wairakei-Tauhara, New Zealand (Allis *et al.*, 2009)).

The economic and environmental impact of land subsidence can be substantial. Land subsidence can disrupt surface drainage, reduce aquifer system storage, create ground fissures and damage properties, farmlands, and infrastructure that may be costly to replace or repair (Schumann *et al.*, 1986; Sheng and Helm, 1998; Feng *et al.*, 2008; Wang *et al.*, 2009). Subsidence can also greatly increase flooding potential in low-lying areas (Potok, 1991; Yong *et al.*, 1991; Dixon *et al.*, 2006; Cabral-Cano *et al.*, 2008).

Detection of land subsidence and monitoring of the spatial and temporal changes of its pattern and magnitude can provide important information about the dynamics of this process and

controlling geological structures. The information can be useful for estimating future subsidence, so measures can be taken to prevent damage to infrastructure and environment.

Detection and monitoring of land subsidence can be accomplished using a number of techniques. Traditional measurements of land subsidence have been conducted using geodetic methods such as precise leveling and geotechnical instruments. Recently, GPS (Global Positioning System) surveys have been widely used. These techniques provide accurate and precise measurements at discrete points on a deforming surface. However, data collection using these techniques is cumbersome, costly, and time consuming. The use of space-borne remote sensing imaging systems for surface deformation detection and monitoring is also possible and could reduce both field work and costs. Using the method known as DInSAR, Differential Interferometric Synthetic Aperture Radar, pairs of images can be processed to obtain high spatial resolution (tens of meters) maps of surface deformation with large spatial coverage (thousands of km^2) and typical accuracy on the order of centimeters (Gabriel *et al.*, 1989; Bürgmann *et al.*, 2000; Hanssen, 2001). Because existing satellite systems have a short repeat cycle on the order of weeks, DInSAR has the potential to resolve time-dependent deformation. The capacity of DInSAR to provide spatially and temporally rich data set turns it into an attractive tool for observing land subsidence.

This paper describes the study of land subsidence in the Mexicali Valley, Baja California, Mexico, where the intense exploitation of the Cerro Prieto Geothermal Field (CPGF) has caused localized subsidence (Glowacka *et al.* 1999, 2005, 2010a, b) and has induced ground fissuring and faulting (Lira, 1996, 1999a, 2005; González *et al.,* 1998; Glowacka *et al.*, 2006, 2010a; Suárez-Vidal *et al.*, 2008). DInSAR measurements from conventional individual two-pass DInSAR and from stack of individual images were analyzed. The results that include the period from December 2004 to December 2005 were compared with available leveling data from 1994-1997 and 1997-2006 in order to evaluate the changes in the subsidence rate and spatial pattern. The observed subsidence pattern was also compared with the tectonic framework of the region to determine if the pattern of subsidence was influenced by faults. Leveling and DInSAR results were modeled to estimate the volume and rate of fluid extraction required to match the observed changes.

2. Studied area

2.1 General information, tectonic and geologic setting

[Insert Figure 1]

The Cerro Prieto Geothermal Field is located in the Mexicali Valley, in the northernmost part of the state of Baja California, Mexico. The Mexicali Valley is part of the Salton Trough tectonic province, which lies on the Pacific-North American plate boundary. The Salton Trough is a depression over 300 km long that extends northwest from the Gulf of California (Figure 1). The Salton Trough has a trans-tensional environment (Herzig and Jacobs, 1994) and includes a system of en-echelon dextral transform faults and pull-apart basins.

Transform faults in the Mexicali Valley include the right-lateral Cerro Prieto and Imperial faults. The sedimentary tensional zone that connects these faults is known as the Cerro Prieto pull-apart basin (Elders *et al.*, 1984; Lippmann *et al.*, 1984; Suárez-Vidal *et al.*, 2008). Several normal faults, oblique to the major faults, have been formed within the basin as consequence of the tensional stress regime imposed by the Cerro Prieto-Imperial fault system (Elders *et al.*, 1984; Lippmann *et al.*, 1984; González, 1999; Suárez-Vidal *et al.*, 2008). The subsurface of the Cerro Prieto basin consists of sediments and metasediments overlying Cretaceous granitic rocks. The sediments include approximately 2700 m of Tertiary sandstones and shales and 2500 m of Quaternary alluvium, mainly gravels, sands, and clays (Lira, 2005). The schematic geological section across Cerro Prieto pull-apart basin is shown in Figure 2a. Localization of the section is indicated in Figure 2b. Thick sedimentary sequences, extensional tectonics, high heat flow, active faults, and abundant groundwater resources from the Colorado River created appropriate conditions for the development of the CPGF geothermal reservoirs.

The CPGF is one of several high-temperature (260-350 °C) water-dominated geothermal fields within the Salton Trough (Elders and Cohen, 1983; Lippmann *et al.*, 1999). The CPGF is operated by Comisión Federal de Electricidad (CFE), Mexico´s state power company, which began power commercial production in 1973 with 75 MWe. Since then, the growth of electricity generation has been achieved by increasing the number of power plants and wells. The newest power plant (CP IV), which is located northeast of existing plants, began operations in 2000 (CFE, 2006). At the present time, the CPGF has a total installed electrical power generating capacity of 720 MWe and is the second largest geothermal field in the world. The geothermal

reservoirs are found at depths varying between 1500 and 3000 m. Currently, about 20 % of the extracted fluid is re-injected at depths of 500-2600 m.

The CPGF is a complex geological and hydrological system. The natural flow through this system is controlled by (1) deltaic layered sedimentary units, (2) major faults, and (3) the regional hydrological pressure gradient (Lippmann and Bodvarsson, 1983). The geothermal reservoirs are recharged by the flow of hot brine from great depths (~5-6 km) in the eastern portion of the field. It is generally accepted that the geothermal reservoirs are also recharged by cold fresh water from shallow aquifers, located to the east, west, and south. This requires rapid downward flow (likely through faults) of cold, low salinity water that recharges the geothermal reservoirs (Halfman *et al.*, 1984; Lippmann *et al.*, 1991; Truesdell *et al.*, 1998; Lippmann *et al.*, 2004; Arellano *et al.*, 2010).

2.2 Subsidence previous studies

The subsidence history in the Cerro Prieto region is well documented. Leveling measurements in the Mexicali Valley began in the 1960's, as part of exploration of the Cerro Prieto geothermal field (Velasco, 1963). These measurements have been carried out up to the present, with varying frequency, precision, coverage, and density. Most were requested by the CFE for monitoring of land elevation in the CPGF and surrounding area (García, 1978; Grannell *et al.*, 1979; de la Peña, 1981; Wyman, 1983; Lira and Arellano, 1997; Glowacka *et al.*, 1999; Lira, 1999b), but some were surveys for tectonic or earthquake studies (Darby *et al.*, 1981, 1984; de la Peña, 1981; Lira, 1996, 1999a, 2006; González *et al.*, 1998).

Based in the analysis of the leveling surveys from 1977 to 1997, Glowacka *et al.* (1999) noticed that the subsidence rate at the center of the field increased after each permanent increase in fluid extraction. A more complete set of data which was recorded during 1994-1997, allowed the estimation of the magnitude and shape of ground surface deformation in the CPGF and surrounding areas. The area of maximum subsidence rate (12 cm/yr) coincided with the location of extraction wells. Another maximum of subsidence rate (9 cm/yr) was located to the east of the field, outside of extraction area. For this reason, the second maximum was interpreted as an area of fluid recharge.

Subsidence in the study area was also studied using DInSAR by Carnec and Fabriol (1999) and Hanssen (2001) using ERS1/2 images acquired in the periods 1993–1997 and 1995-1997,

respectively. Significant local subsidence up to 1.5 cm/month was detected. Although agricultural activity in the area limited the area of investigation, the results revealed that the ground deformation is associated with the extraction of geothermal fluid and agreed with the leveling data.

Field mapping performed since 1989 in the surrounding CPGF area shows that many of the subsidence-induced fractures, fissures, collapse features, small grabens, and vertical displacements are closely related to the known tectonic faults (Gonzalez *et al.*, 1998; Glowacka *et al.*, 2006, 2010a; Lira, 2006; Suárez-Vidal *et al.*, 2007, 2008). This information is summarized in the Figure 2b. The affected area is localized between the Cerro Prieto and the Morelia faults to the NW, and the Imperial and Saltillo faults to the SE, which limit the Cerro Prieto pull apart basin (Suárez-Vidal *et al.*, 2008).

Measurements using geotechnical instruments indicate that slip is accommodated mainly by aseismic creep along these faults (Glowacka *et al.*, 2010a, b). Analysis of the extension, amplitude, and temporal behavior of the slip on the Cerro Prieto and Saltillo fault suggest that these faults constitute a boundary of the actively subsiding area, and likely constitute a groundwater barrier.

Using a tectonic model of the pull-apart center, and GPS measurements of tectonic motion (Bennett *et al.*, 1996), Glowacka *et al.* (2005) estimated that the tectonic subsidence is responsible for only 4-5% of the measured subsidence, leaving some 95% to anthropogenic causes. This agrees with independent estimates by Camacho Ibarra (2006), who suggested that 82-90 % of the observed subsidence in this region is anthropogenic. For this estimation Camacho Ibarra (2006) compared ground height changes data from leveling and GPS surveys over the period of 1962-2001 and modeled the coseismic tectonic deformation.

Several efforts have been conducted to model the observed deformation. Carnec and Fabriol (1999) and Hanssen (2001) approximated it by using a spherical hydrostatic sources embedded in an elastic half space (Mogi, 1958) while Sarychikhina (2003) and Glowacka *et al.* (2005, 2010a) used a rectangular tensional crack in an elastic half-space (Yang and Davis, 1986). The location and depth of the best-fit models suggest that the observed surface deformation can be related to geothermal fluid extraction.

3. Data

As mentioned above, the land subsidence in the Mexicali Valley area is monitored by periodical leveling surveys. In addition, geological reports from different projects that have surveyed the area are available (Gonzalez *et al.*, 1998; Glowacka *et al.*, 2006, 2010a; Lira, 2006; Suárez-Vidal *et al.*, 2007, 2008). In this study, in an attempt to supplement the surface observations and to gain an improved understanding of the temporal and spatial distribution of surface deformation, the data from ground-based techniques were combined with DInSAR data.

Two datasets of second-order, first class leveling surveys (6 mm/km$^{1/2}$ accuracy) were used in this paper. The first, and most complete, set of precise leveling data was recorded during the 1994-1997 period (Lira and Arellano, 1997; Glowacka *et al.*, 1999). After discarding the data from benchmarks with evidently erroneous measures, this leveling dataset comprises 95 benchmarks. The reference point, assumed to be stable, is located to the SE of the study area, in the Cucapah ranges (benchmark "10004") (Figure 2b).

The second leveling dataset consists of data collected during two campaigns in 1997 and 2006 (Glowacka *et al.*, 2006) using the same benchmarks network as for the first leveling dataset. After discarding the data from benchmarks with evidently erroneous measures and those strongly affected by displacement caused by 24 May, 2006 Mw=5.4 earthquake (Sarychikhina *et al.*, 2009), this dataset comprises data from 67 benchmarks reporting the vertical displacement relative to the reference fixed point (benchmark "10037") (Figure 2b). The different reference points for these datasets is due to the loss, probably by destruction, of benchmark "10004" sometime between 1997 and 2006. Benchmark "10037" is also located to the SE of the study area, ~3.5 km northeast from the benchmark "10004" (Figure 2b). To compare both datasets we referenced the first 1994-1997 dataset to the benchmark "10037".

[Insert Figure 2– color web and paper]

Radar differential interferometry technique is based on the difference of two Synthetic Aperture Radar (SAR) images acquired for the same area at different times from slightly different positions. The result of this combination is a new image known as interferogram, whose main phase component, after corrections for topography and earth curvature, is the ground displacement along the radar line of sight (LOS). For an introduction to the DInSAR method, see

Gabriel *et al.* (1989), Massonnet and Rabaute (1993), Gens and van Genderen (1996), Massonnet and Feigl (1998), Rosen *et al.* (2000) and Hanssen (2001).

In this study, data from the ENVISAT ASAR system have been used to analyze the subsidence of the study area. The ENVISAT ASAR, which began operation in 2002, is a C-band sensor with an average (scene center) incidence angle of 23° and 35 days revisit. Because of the steep incidence angle of ENVISAT radar, the interferograms are most sensitive to the vertical component of the deformation.

A total of 22 Single Look Complex (SLC) images were acquired. The SAR images covered the time period between October 2003 and May 2006[1]. Among the images, 17 were from the descending track and 5 from ascending track (Table 1). Data from ascending and descending passes have different imaging geometry (look direction), providing two linearly independent LOS measurements. The spatial coverage of these images is presented in Figure 1.

[Insert Table 1]

4. DInSAR data analysis

4.1 Interferograms processing and analysis

Interferometric processing was performed using the public domain DORIS InSAR package developed at the Delft Institute for Earth-oriented Space Research (Kampes *et al.*, 2003). Precise DEOS satellite orbits (Scharroo and Visser, 1998) and the 3-arcsecond Shuttle Radar Topography Mission (SRTM) digital elevation model were used during processing. All interferograms were multi-looked 4 times in range and 20 times in azimuth, resulting in a final pixel size of approximately 100 m by 100 m. Adaptive filtering (Goldstein and Werner, 1998) was applied to each interferogram.

All the possible interferometric pairs combinations with perpendicular baseline shorter than 400 m were analyzed (Sarychikhina, 2010). Figure 3 shows the perpendicular baseline information with respect to the first acquisition of each dataset. Parameters of the interferometric pairs presented in this paper are shown in the Table 2.

[1] There were no earthquakes with magnitude greater than 5 (M≥5) in the study area in this period.

[Insert Figure 3]

[Insert Table 2]

The interferograms were visually examined to identify problems caused by decorrelation and atmospheric effects. The highly vegetated areas surrounding the CPGF cause significant phase decorrelation of the C-band SAR pairs over periods of time longer than 3 months (105 days), due to the seasonal growth and the movements caused by the wind on the grown plants. By contrast, the mainly desert area of the CPGF maintains high levels of coherence over longer time intervals (Figure 4).

Figure 4 shows geocoded differential interferograms constructed using the two-pass method. All differential interferograms show poorly to fairly well-defined fringes with a common geographic location. As this feature was observed on independent interferograms, it is likely not due to atmospheric effects, which vary in time, but to ground deformation. Despite the difference in imaging geometry, fringe patterns appear similar in the ascending and descending interferograms (Figure 4). In the differential interferograms from ascending and descending passes a clear elliptical northeast-southwest directed fringe pattern is observed and the phase gradient indicates an LOS displacement of the surface away from the satellite. This similarity between ascending and descending interferograms along with the known vertical displacement from ground-based measurements including leveling surveys suggest that the observed LOS displacements may be interpreted as reflecting mostly vertical surface subsidence.

In the highest quality interferograms, two regions of highest subsidence occur within the larger elliptical zone (Figure 4). The first centre of subsidence is located in the CPGF production zone (e.g. Figure 2b). The second is located in the area between the eastern limits of the CPGF and the Saltillo fault, which was proposed as recharge zone in previous studies (Glowacka *et al*., 1999, 2005; Sarychikhina, 2003).

The area affected by subsidence coincides largely with the shape of the Cerro Prieto pull-apart basin described by Suárez-Vidal *et al.*, (2008). The subsiding area boundaries appear to correlate with faults and/or fissures zones as can be seen in Figure 4. The subsidence ceases abruptly toward the southeast and east at the Saltillo fault. The Cerro Prieto fault limits the subsiding area in the southwest. The subsidence observed along the Saltillo fault is much more abrupt than in

the Cerro Prieto fault. This agrees with observations from vertical crackmeter and a 3-D witness[2] installed on Saltillo and Cerro Prieto fault, respectively (Glowacka *et al.* 2010a, b). The Morelia fault and the fractures zone that continue toward the Imperial fault mark the northern limit of subsidence. The deformation appears less severe south and southeast of the fissure zone, which appears to be a continuation of the Saltillo fault, as proposed by Suárez-Vidal *et al.* (2008), and named here SF' (Figure 4). Note that the influence of the Saltillo-Guerrero graben is not observed in the differential interferograms.

Besides the persistent pattern described above which is apparent on all interferograms, a smaller circular fringe pattern is observed south of the evaporation pond in the 2004/12/19-2005/02/27 and 2005/02/27-2005/06/12 interferograms (Figure 4c and d). This fringe pattern is also observed in several other interferograms processed but not shown here. However, the polarity of surface deformation (subsidence or uplift) indicated by this fringe pattern varies for different interferograms. In the interferograms 2004/12/19-2005/02/27 and 2005/02/27-2005/06/12 (Figure 4c and d) the fringe pattern indicates a decrease in range or surface uplift. Carnec and Fabriol (1999) observed a similar pattern which indicates a decrease in range for 1995/12/16-1996/05/04 interferograms. They attributed this decrease in range to uplift related to the reinjection of waste fluid at the southern end of the evaporation pond, because the central part of the observed bowl shaped pattern is located 3 km south of three reinjection wells. However, Hanssen (2001) attributed this fringe pattern to atmospheric artifacts. The consistent occurrence of this pattern would argue against the atmospheric effects but the variation in polarity is puzzling, unless the reinjection rate varies greatly, which might produce this effect. Seasonal changes in ground deformation polarity (seasonal subsidence and uplift) were observed by Bawden *et al*. (2001) in Santa Ana basin, Lu and Danskin (2001) in Bernardino basin, Watson *et al.* (2002) in Los Angeles basin, California, and Hoffmann *et al.* (2001) in Las Vegas Valley, Nevada.

Except for the described small circular fringe pattern south of the evaporation pond, the regions surrounding Cerro Prieto pull-apart basin do not show any significant signs of surface deformation and consequently are considered stable for the purposes of this study. Some local

[2] 3-D witness (Deformation Gages) measures 3 components of the slip vector on the fault, registering the relative displacement between 2 benchmarks located in the opposite sides of the fault. 3-D witness is not a digital instrument, and the measurements are taken manually by the technical personnel during the field works, approximately once in 1 to 3 months.

phase gradients outside of the subsidence area may be due to residual topographic or atmospheric noise. Topography-related artifacts in interferograms are observed in the area of Cerro Prieto volcano and the foothills of the Cucapah Mountains (SW corner) (Figure 4). These phase changes are likely due to topography or/and layered atmosphere because the magnitude of the signal increases with increases in perpendicular baseline (Table 2). Similar effects are not expected in other parts of interferograms because the rest of the study area has flat topography. Spatial variations in the atmospheric conditions seem to be responsible for essentially random perturbations in the radar phase difference in the interferograms, e.g. strong radar phase difference signal east to the Imperial fault in the 2005/09/25-2005/12/04 interferogram (Figure 4f).

[Insert Figure 4– color web and paper]

4.2 Interferograms stacking

One way to reduce noise that is randomly distributed in time (such as atmospheric noise) is by stacking interferograms. Stacking differential interferograms involves the summing multiple differential interferograms into a single interferogram and then dividing by the total time. This will yield a yearly rate of deformation. Four differential interferograms with temporal separations between 70 and 105 days (Figure 4 c-f) and covering successive periods were selected for stacking.

Before stacking the phase of each interferogram was first unwrapped using a statistical minimum-cost flow algorithm implemented in the SNAPHU package (Chen and Zebker, 2001). The unwrapped interferograms were detrended to compensate for orbital errors, converted to the LOS displacement and then referenced to a common point in the space. The common reference point is the benchmark "10037" from the 1997-2006 leveling data (Figure 5). The stack covered a period of 350 days between December 2004 and December 2005 (Figure 6a). Pixels that were decorrelated on any interferogram were not included in the stack.

The subsidence pattern of the resulting LOS displacement map is similar to the pattern obtained in individual interferograms. The subsiding area is correlated with the area of the Cerro Prieto pull-apart basin. As it can be seen in Figure 6a, the maximum estimated deformation rate is ~16

cm/yr, and occurs in the recharge zone. The maximum deformation rate in the CPGF production zone is ~10 cm/yr.

4.3 Data error estimation

The expected accuracy of the LOS displacement rate obtained from the stacked interferogram, Δv_{LOS}, was computed as proposed by Strozzi *et al.* (2001):

$$\Delta v_{LOS} = \frac{\sqrt{n}E}{t_{cum}}. \qquad \text{Eq. (1)}$$

Here, n is the number of interferograms used for stacking, t_{cum} is the total time interval covered by stacking, and E is the assumed phase error of a single interferogram. There is no straightforward method to estimate observation error for the single interferogram. In this study the observation error for each interferogram used in the stacking was estimated from the residuals in the assumed stable area. These residuals correspond to non-displacement related interferometric disturbances induced mainly by DEM inaccuracies and noise in the differential interferograms. A triangular area (~90 km^2) located to the south-east from the evaporation ponds was assumed stable (Figure 5). This area is located very close to the Cucapah Mountains and outside the limits of the pull-apart Cerro Prieto basin, where the reference benchmark for leveling surveys is located and was considerate stable by Glowacka *et al.*, (1999; 2001). The RMS error for each interferogram was calculated (Table 3) and the average RMS error of 0.7cm was used to calculate LOS displacement rate accuracy of the stacking. Using Equation (1) the expected LOS displacement rate estimation error of approximately ± 1.5 cm/yr was obtained.

[Insert Table 3]

[Insert Figure 5– color web and paper]

[Insert Figure 6– color web and paper]

4.5 Modeling of DInSAR data.

The subsidence indicates volume contraction within the reservoir. Therefore surface deformation could be modeled assuming a volume change at depth. Mossop and Segall (1997) used a point pressure source in an elastic half-space (Mogi, 1958) to model subsidence in the Geysers

geothermal field. Carnec and Fabriol (1999) and Hansen (2001) used the same approach to model subsidence in the CPGF. Fialko and Simons, (2000) assumed a deflating triaxial ellipsoidal cavity (Davis, 1986) to model subsidence in the Coso geothermal field. More sophisticated models are those of Segall (1989) and Walsh (2002) that use a poroelastic framework and slightly more complicated reservoir geometry.

However, none of these models address all of the complexities presented in the CPGF (Sarychikhina, 2003). We chose to use a model of a dipping rectangular tensional crack embedded in an elastic half-space (Yang and Davis, 1986; Okada, 1992) as it seems to be more appropriate for the CPGF reservoirs, which are tilted sedimentary layers bounded by faults. This model assumes that the surface deformation is caused by a tensile component of displacement, such as the opening or closing of a tabular or crack-like body. The closing or opening of the crack corresponds to an appearance or a disappearance of volume of material in the plane of the crack (2-D crack). This volume is given by the area of the crack multiplied by an opening or a closing of the crack. The crack closing is equivalent to reservoir or aquifer contraction due to fluid withdrawal.

The model of a dipping rectangular tensional crack was used by Sarychikhina (2003) and Glowacka *et al.* (2005) to model subsidence in the CPGF detected by 1994-1997 leveling surveys. Each crack is characterized by a series of geometrical parameters such as its center location (*x, y, z*), length (*L*), width (*W*), azimuth (*Azm*.), dip (*Ang.*) and closing (*p*).

The technique was also used to model the 2004-2005 DInSAR data. A forward modeling process similar to the one performed by Glowacka *et al.* (2005) was applied to find the rectangular tensional cracks that fit the best the observed LOS displacement field. The modeling was performed using the Coulomb 3.1 software (Lin and Stein, 2004; Toda *et al.*, 2005). Initial parameters were based on results from 1994-1997 leveling data model (Glowacka *et al.*, 2005), a hydrological model of the CPGF (Halfman e*t al.,* 1984; Lippmann *et al.*, 1991), and information about location of surface fissures and faults from geological surveys (González *et al.*, 1998; Glowacka *et al.*, 2010a; Suárez-Vidal *et al.*, 2008).

The calculated vertical, D_U, easting, D_E, and northing, D_N, components of the surface displacement vector were converted into line-of-sight displacement (i.e. range change, ΔR,) during the modeling using the expression for a LOS acquired in a right looking direction in a descending track (Fialko *et al.*, 2001), which is:

$$\begin{bmatrix} -\cos(\theta) & -\sin(\theta)\cos(\alpha) & \sin(\theta)\sin(\alpha) \end{bmatrix} \begin{bmatrix} D_U \\ D_E \\ D_N \end{bmatrix} = \begin{bmatrix} \Delta R \end{bmatrix}, \quad \text{Eq. (2)}$$

where θ and α are the look angle and azimuth of the satellite heading vector, respectively.

The synthetic LOS displacement field was compared with the observed LOS displacement data. The parameters of the best-fit model are presented in Table 4. The best fit model consists of seven closing cracks representing different reservoirs and aquifers of CPGF: four cracks represent geothermal reservoirs α_1,α_2,β_1 and β_2, and three represent recharge aquifers *sr* (small recharge) ,*LR1* (large recharge) and *LR2*, as continuation of *LR1*.. The cracks of the best-fit model are superimposed on the schematic geological section across Cerro Prieto pull-apart in Figure 2a. Observed and modeled LOS displacement rates are presented in the Figure 6.

The calculated LOS displacements are shown in Figure 6b with the rectangular tensional cracks corresponding to the best fitting solution. Figure 6c shows the predicted LOS displacement field with area of low coherence masked out. Figure 6d shows a residual after subtracting the best fitting model from the data, and Figure 7 shows three profiles across the subsidence zone with the observed and modeled LOS displacements. Both the shape and magnitude of the modeled surface LOS displacement are quite similar to the observed ones. The absolute value of the residual at most observation points is 0.0 – 1 cm/yr, smaller than the presumed error, although local discrepancies show as much as 5 cm/yr. The nature of these local discrepancies is discussed in the next section. The root mean square error per observation point (RMS) of the best-fit model is 1.0 cm/yr.

While the initial model was based on the 1994-1997 model, the final DInSAR best-fit model differs from that one. First, more cracks were required to fit the data. The α reservoir is represented in our model by two cracks: α_1 and α_2, instead of a single one as was done in 1994-1997 model. This supposition is in better agreement with hydrological and geological data of the CPGF which suggest that the α reservoir, shallower CPFG geothermal reservoir located in the West of the production zone, is divided in two parts by normal SE-dipping H fault (e.g. Ocampo Díaz and De León, 2003). *LR2* was added to *LR1* crack to model the complex form of the subsidence pattern in the southern zone. In 1994-1997 no leveling benchmarks existed in this zone.. The depth of *sr* crack center was increased from 1500 to 2800 m, first, to be in better

agreement with the geological model and, second, to explain the depth range of slip events proposed by Glowacka *et al.* (2010a).

[Insert Table 4]

[Insert Figure 7]

5. Comparison of leveling surveys with DInSAR data.

We compared the deformation rate obtained by the DInSAR stacking method with 1994-1997 and 1997-2006 leveling results (Glowacka *et al.*, 1999, 2006), in order to evaluate the changes in the spatial pattern and rate of land subsidence. The velocity contour maps in cm/yr from the leveling data, projected to the LOS direction using Equation (2) and considering only the vertical displacement component, are shown in Figure 8a and b. The contours were obtained by interpolation of the data using the Kriging algorithm. The leveling data from the 1994-1997 survey were referenced to the reference benchmark for 1997-2006 survey ("10037").

The 1994-1997 leveling survey shows a maximum LOS displacement rate of ~10 cm/yr in the center of the CPGF production zone and ~8 cm/yr in the recharge zone (Figure 8a). The 1997-2006 leveling survey indicates an increase in LOS displacement rate in the recharge area reaching a value of ~12 cm/yr (Figure 8b). The LOS displacement rate in the production CPGF zone decreased to ~9 cm/yr in the same period of time. However, fewer benchmarks were used over the production zone during the later time period and it is possible that the reduction is an artifact caused by the sparser data (Figure 8a and b).

Figure 8c shows the velocity contour plot in cm/yr from the DInSAR data for 2004-2005. Figure 8 reveals that the subsidence in the recharge zone, increased by a factor of ~1.5 between 1997 and 2005. The magnitude of maximum subsidence in the CPGF extraction zone did not change during this period of time; however, its locus migrated to the northeast. To ensure that the observed changes in the LOS displacement pattern are real effects and not artifacts caused by different techniques, the velocity contour map from DInSAR data using only the pixels at the location of the 1994-1997 leveling benchmarks was drawn (Figure 8d). If a pixel value was indeterminate, the value from nearest pixel (distance less than 500 m) was taken instead. Total number of 64 values was used. The results suggest that the observed changes in pattern and rate of subsidence are not artifacts.

Next, we model the subsidence reported by 1994-1997 leveling data using the new cracks model obtained in section 4.3 to check its robustness. The rationale behind this idea is that the same cracks are responsible for the subsidence in the study area at different time. Therefore we assumed that the cracks location and geometry are time independent (defined by tectonic and/or geology of the area) and the amount of cracks closing can change in time depending on the extraction rate. The results are shown in Figure 9 and the parameters of the model are shown in Table 4. The best fit model has a RMS of 1 cm/yr. The residuals in most of the leveling benchmarks range between 0 and 2 cm/yr. However, large residuals, up to 4 cm/yr, are observed in three benchmarks located in the western border of evaporation pond. The leveling data suggests that this zone is subsiding; whereas the DInSAR suggests that this zone is practically stable (Figure 8). Unfortunately, the leveling survey data from 1997-2006 does not include these benchmarks for comparison. However, a differential interferogram obtained by Carnec and Fabriol (1999) using ERS 1 images acquired in 16/12/1995 and 04/05/1996 clearly shows that this zone is practically stable. Based on this result we suspect that the more likely explanation of observed discrepancy is movement or disruption of those benchmarks during the repair of the evaporation pond borders, which occurs frequently. As no confirmation of this is available, it may also be due to a subsurface effect such as change in the hydrological regime.

In the calculations it was assumed that the change in volume of every particular crack is equivalent to the volume removed from (or added to) the corresponding reservoir/aquifer/aquitard (without analyzing details of the compaction phenomenon). With this assumption, using the estimated values of the crack dimensions and their closing, the volume change in the reservoirs and aquifers was evaluated for two periods: 1994-1997 and 2004-2005 (Table 5). From Table 5 it can be seen that volume change in 2005 period is ~15% more than for 1994-1997 which is comparable with net extraction (extraction-injection) change, which is about 18% larger for 2005 period, comparing with net extraction in 1994-1997 (Figure 10).

[Insert Table 5]

[Insert Figure 8 – color web and paper]

[Insert Figure 9 – color web and paper]

[Insert Figure 10]

6. Results and discussion

In this paper, a differential interferometric analysis using C-band radar data was conducted to map the extent and pattern of the anthropogenic subsidence of the Mexicali Valley near the Cerro Prieto geothermal area. The differential interferograms clearly show a deformation signal with a time span of up to 1 year. Temporal decorrelation in vegetated area decreased coherence significantly for time periods of more than three months and atmospheric noise was also a problem. Despite the problems a consistent deformation pattern was revealed.

Four successive short time span interferograms were stacked in order to obtain a longer time period interferogram and reduce random noise. The stacked interferogram covers December 2004–December 2005 period and the estimated accuracy of DInSAR LOS displacement rate derived from the stacking is ±1.5 cm/yr.

The analysis of DInSAR data from ascending and descending tracks combined with ground based data shows that the DInSAR LOS deformation signal is mainly due to vertical subsidence. DInSAR observations confirm that the total area of ground deformation appears as a roughly NE-SW oriented elliptical-shaped feature with two bowls exhibiting high LOS deformation rates in the December 2004–December 2005 period: ~16 cm/yr in the recharge zone (east – northeast of the study area) and ~10 cm/yr below in the east boundary of CPGF production zone, which corresponds to ~17 cm/yr and ~11 cm/yr of subsidence, respectively. The DInSAR mapping also shows that the spatial extent of the subsidence matches the location of known tectonic faults. Therefore it appears that these faults control the spatial extent of the observed subsidence, and constitute, probably, groundwater flow barriers for aquifers/reservoirs. The shape of the subsiding area also correlates with the Cerro Prieto pull-apart basin.

Several individual interferograms revealed a small zone of deformation south of the evaporation pond. The polarity of the deformation varies for different interferograms. This signal was observed earlier but attributed to either recharge (Carnec and Fabriol, 1999) or atmospheric artifacts (Hansen, 2001). Given the consistency of the signal over time, atmospheric artifacts seem unlikely but the change in polarity is difficult to explain. Possibly the recharge and/or injection rate varies significantly which might cause these variations.

The DInSAR LOS displacement was modeled using a series of rectangular tensional cracks embedded in an elastic half-space. The model is based on hydrological model of the CPGF and

includes the information of rupture and fissure zones from geological survey and well data. The final model consists of seven rectangular cracks. Four of them correspond to geothermal reservoirs; the remaining three represent recharge aquifers. Comparison of the observed and modeled surface displacements shows a reasonable agreement (RMS per observation point is 1.0 cm/yr, less than the presumed error of DInSAR LOS displacement rate) but does not explain all the features. An area with large residuals is located in the eastern side of the Saltillo fault, which is a fluid flow barrier and subsidence boundary. This fault has a curved shape which is not matched with the applied model of rectangular tensional crack.

Based on observed subsidence pattern and/or results of modeling, three new geological features are proposed (Figure 11). The first proposed feature (F1) is a fault which appears to be the limit of the subsiding area to the northwest. This limit might be Cerro Prieto fault, Morelia fault or an unknown fault (Figure 11). The pond prevents definite identification of the fault by ground-based or remote-sensing techniques and a technique such as a chirp seismic reflection survey would be necessary. The second proposed feature (F2) is a fault which limits the α_2 crack to the south and could be one of several normal faults, oblique to the major faults, of the Cerro Prieto pull-apart basin. This fault does not rupture the surface. However, the ground fissuring in this zone is an additional evidence of a sub-surface fault. The best-fit model and the observed subsidence pattern also suggest the existence of other buried structures (F3) within and below the aquifer-bearing sedimentary basin fill, between the eastern edge of CPGF (β_1 and β_2 cracks from the model) and the recharge zone (*sr* crack from the model). This structure appears to have a linear form, parallel to the principal faults: the Cerro Prieto and the Imperial faults (Figure 11). The formation of two separate centers of subsidence is suggested by the model of pull-apart basin development (Aydin and Nur, 1982). Therefore, the origin of the observed structure is tectonic. However it is difficult to determine if this limit between two subsidence basins is only stratigraphic or also represents a faulting zone.

[Insert Figure 11 – color web and paper]

A comparison of the deformation rates obtained using different techniques and time intervals indicate that the average rate of deformation has increased since 1997. The maximum increase of deformation rate is observed in the recharge zone. Also the center of deformation in the CPGF

production zone is migrating to the northeast. These results suggest that the subsidence in the study area is a dynamical process. The changes in the ground deformation pattern may be caused by production increase in the CPGF due to the newest power plant (CP IV) which started operating in 2000 in the eastern part of field (Figure 2b), as was suggested by Sarychikhina *et al.* (2007) and Glowacka *et al.*, (2010a). Modeling results show correlation between the increase of subsidence rate and net extraction increase.

7. Conclusions

The integrated analysis of satellite observations, ground-based geological and geodetic measurements was performed in this study in order to improve the understanding of temporal and spatial distributions of anthropogenic subsidence in the Mexicali Valley related to the extraction of geothermal fluids in the CPGF. The changes in subsidence spatial pattern and rate are highly correlated with the development of the CPGF. However the spatial extent of the observed subsidence is controlled by faults.

Based on this study, it is expected that future increase of extraction rate and field limits expansion, as proposed by Aguilar Dumas (2010), would likely lead to additional future subsidence. So the evaluation of geological and environmental hazard due to subsidence process is required for Mexicali Valley area.

As mentioned before subsidence causes damage to infrastructure. In the case of the Mexicali Valley, situated in the desert climate of the Colorado River delta, the urban and agricultural water depend on a system of canals transporting water from the Colorado River. The subsidence and related problems (i.e. ground fissures and fractures) affect the efficiency of water distribution system and significantly increase the cost of canals maintenance. They also affect the cost of maintenance of the agricultural fields, roads and railroad.

The deep fluid extraction also can change the stress level, and influence seismicity of the area. This phenomenon, suggested for oil and gas extraction (e.g. Segall, 1989) was analyzed for CPGF by Glowacka *et al*. (1999, 2005).

The DInSAR technique, together with field observations, allow to measure subsidence rate, identify areas with maximum subsidence rate, and observe the subsidence rate changes with time. Using these data, mathematical modeling presented in this work, and plan for future CPGF

development, the spatial distribution of the subsidence rate can eventually be forecast, which allows to take technical and economical decisions about future investments and analyze possible way of subsidence prevention.

Acknowledgments

The European Space Agency's ENVISAT satellite was used to collect the interferometric data. The data were obtained as part of ESA Cat-1 Project (ID - C1P3508).
This research was sponsored in part by CONACYT, project number 45997-F, CONAGUA, agreement GRPBC-CICESE-01, and CICESE internal funds. The first author was sponsored by the Ministry of Foreign Affairs of Mexico (SRE) PhD scholarship.
The opinions expressed in this paper are solely the authors' and do not necessarily express the point of view of Mexican Federal Electricity Commission which operates CPGF.
The authors thank the two anonymous reviewers for their helpful comments and valuable suggestions that led to improve and clarify the manuscript.

Reference

Aguilar Dumas, A., 2010. Situación actual y alternativas de exploración y explotación en el campo geotérmico de Cerro Prieto, BC. Geotermia, 23(2), 33-40.

Allis, R.G., Bromley, C.J. and Currie, S., 2009. Update on subsidence at the Wairakei–Tauhara Geothermal System. Geothermics, 38, 169–180.

Arellano, V.M., Barragán, R.M., Aragón, A., Izquierdo, G., Portugal, E., Rodríguez, M.H. and Alfredo Pérez, A., 2010. Reservoir Characteristics and Exploitation-Related Processes at the CP IV Sector of the Cerro Prieto (México) Geothermal Field. In Proceedings of the World Geothermal Congress 2010, Nusa Dua, Bali, pp. 1-6.

Aydin, A. and Nur, A., 1982. Evolution of pull-apart basin and their scale independence. Tectonics, 1, 91-105.

Bawden, G.W., Thatcher, W., Stein, R.S., Hudnut, K. W.and Peltzer, G., 2001. Tectonic contraction across Los Angeles after removal of groundwater pumping effects. Nature, 412, 812-815.

1 Bennett, R.A., Rodi, W. and Reilinger, R.E., 1996. Global Positioning System constraints on
2 fault slip rates in southern California and northern Baja, Mexico. Journal of Geophysical
3 Research, 101(B10), 21943-21960.
4 Bürgmann, R., Rosen, P.A. and Fielding, E.J., 2000. Synthetic aperture radar interferometry to
5 measure Earth's surface topography and its deformation. Annual Review of Earth and
6 Planetary Sciences, 28(1), 169-209.
7 Cabral-Cano, E., Dixon, T.H., Miralles-Wilhelm, F., Díaz-Molina, O., Sánchez-Zamora, O. and
8 Carande, R.E., 2008. Space geodetic imaging of rapid ground subsidence in Mexico City.
9 Geological Society of America Bulletin, 120(11-12), 1556.
10 Camacho Ibarra, E., 2006. Análisis de la deformación vertical del terreno en la región de
11 confluencia del sistema de fallas Cerro Prieto - Imperial en el periodo 1962-2001. M.Sc.
12 Thesis, Centro de Investigación Científica y Educación Superior de Ensenada, Ensenada,
13 B.C., Mexico, 135 pp.
14 Carnec, C. and Fabriol, H., 1999. Monitoring and modeling land subsidence at the Cerro Prieto
15 geothermal field, Baja California, Mexico, using SAR interferometry. Geophysical
16 Research Letters 26(9), 1211-1214.
17 CFE, 2006. Cerro Prieto Geothermal Field., CFE, Residencia General de Cerro Prieto.
18 Chen, C.W. and Zebker, H.A., 2001. Two-dimensional phase unwrapping with use of statistical
19 models for cost functions in nonlinear optimization. Journal of the Optical Society of
20 America, 18(2), 338-351.
21 Darby, D., González, J. and Lesage, P., 1984. Geodetic studies in Baja California, Mexico, and
22 the evaluation of short-range data from 1974 to 1982. Journal of Geophysical Research,
23 89(B4), 2478-2490.
24 Darby, D., Nyland, E., Suárez-Vidal, F., Chavez, D. and González, J., 1981. Strain and
25 displacement measurements for the June 9, 1980 Victoria, Mexico, Earthquake.
26 Geophysical Research Letters, 8(6), 549-551.
27 Davis, P. M., 1986. Surface deformation due to inflation of an arbitrarily oriented triaxial
28 ellipsoidal cavity in an elastic half-space, with reference to Kilauea Volcano, Hawaii.
29 Journal of Geophysical Research, 91, 7429–7438.
30 de la Peña, L., A., 1981. Results from the first order leveling surveys carried out in the Mexicali
31 Valley and at the Cerro Prieto field, Baja California, the Third Symposium on the Cerro

Prieto Geothermal Field, Baja California, Mexico, Lawrence Berkeley Laboratory, Berkeley, California, pp. 281-291.

Dixon, T. H., Amelung, F., Ferretti, A., Novali, F., Rocca, F., Dokka, R., Sella, G., Kim, S., Wdowinski, S. and Whitman, D., 2006. Space geodesy: Subsidence and flooding in New Orleans. Nature, 441, 587-588.

Elders, W.A. and Cohen, L.H., 1983. The Salton Sea Geothermal Field, California, as a Near-Field Natural Analog of a Radioactive Waste Repository in Salt. Technical Report BMI/ONWI-513, Institute of Geophysics and Planetary Physics, University of California, Riverside, 146 pp.

Elders, W.A., Bird, D.K., Williams, A.E. and Schiffman, P., 1984. Hydrothermal-flow regime and magmatic heat source of the Cerro Prieto geothermal system, Baja California, Mexico. Geothermics, 13, 27-47.

Feng, Q.Y., Liu, G.J., Meng, L., Fu, E.J., Zhang, H.R. and Zhang, K.F., 2008. Land subsidence induced by groundwater extraction and building damage level assessment—a case study of Datun, China. Journal of China University of Mining and Technology, 18(4), 556-560.

Fialko, Y. and Simons, M., 2000. Deformation and seismicity in the Coso geothermal area, Inyo County, California: Observations and modeling using satellite radar interferometry. Journal of Geophysical Research, 105(B9), 21,781-21,794.

Fialko, Y., Simons, M. and Agnew, D., 2001. The complete (3-D) surface displacement field in the epicentral area of the 1999 Mw 7.1 Hector Mine Earthquake, California, from space geodetic observations. Geophysical Research Letters, 28, 3063–3066.

Gabriel, A., Goldstein, R. and Zebker, H., 1989. Mapping small elevation changes over large areas: Differential radar interferometry. Journal of Geophysical Research, 94(B7), 9183–9191.

García, J.R., 1978. Estudios de nivelación de primer orden en Cerro Prieto, the First Symposium on the Cerro Prieto Geothermal Field, Baja California, México, pp. 148-150.

Gens, R. and van Genderen, J.L., 1996. SAR interferometry: issues, techniques, applications. International Journal of Remote Sensing, 17(10), 1803-1835.

Glowacka, E., González, J. and Fabriol, H., 1999. Recent vertical deformation in Mexicali Valley and its relationship with tectonics, seismicity, and the exploitation of the Cerro Prieto geothermal field, Mexico. Pure and Applied Geophysics, 156(4), 591-614.

Glowacka, E., González, J.J., Nava, F.A., Farfán, F. and Díaz de Cossío, G., 2001. Monitoring Surface Deformations in the Mexicali Valley, B.C., Mexico. In Proceedings of tenth International Symposium on Deformation Measurements, Orange, California, USA, pp. 175-183.

Glowacka, E., Sarychikhina, O. and Nava, A.F., 2005. Subsidence and stress change in the Cerro Prieto Geothermal Field, B.C., Mexico. Pure and Applied Geophysics, 162, 2095–2110.

Glowacka, E., Sarychikhina, O., Suárez, F., Mendoza, R. and Nava, F.A., 2006. Estudio geológico para definir la zona de hundimiento con el fin de relocalización del canal Nuevo Delta en el Valle de Mexicali. Informe Técnico, CICESE, México, 505 pp..

Glowacka, E., Sarychikhina, O., Suárez, F., Nava, F.A. and Mellors, R., 2010a. Anthropogenic subsidence in the Mexicali Valley, Baja California, Mexico, and slip on the Saltillo fault. Environmental Earth Sciences, 59(7), 1515-1524.

Glowacka, E., Sarychikhina, O., Suárez, F., Nava, F.A., Farfan, F., Batani, G., and Garcia Arthur, M. A., 2010b, Anthropogenic subsidence in the Mexicali Valley, B.C., Mexico, caused by the fluid extraction in the Cerro Prieto Geothermal Field, and the role of faults. In Proceedings of the World Geothermal Congress 2010, Nusa Dua, Bali, pp. 1-4.

Goldstein, R.M. and Werner, C.L., 1998. Radar interferogram filtering for geophysical applications. Geophysical Research Letters, 25(21), 4035-4038.

González, J., Glowacka, E., Suárez, F., Quiñones, J.G., Guzmán, M., Castro, J.M., Rivera, F. and Félix, M.G., 1998. Movimiento reciente de la Falla Imperial, Mexicali, B. C. Ciencia para todos Divulgare, Universidad Autónoma de Baja California, 6(22), 4-15.

González, M., 1999. Actualización del modelo del basamento en el campo geotérmico de Cerro Prieto, BC, México. Geotermia, 15(1), 19–23.

Grannell, R.B., Tarnman, D.W., Clover, R.C., Leggewie, R.M., Aronstam, P.S., Kroll, R.C. and Eppink, J., 1979. Precision gravity studies at Cerro Prieto - the second year, the Second Symposium on the Cerro Prieto Geothermal Field, Baja California, Mexico, Lawrence Berkeley Laboratory, Berkeley, California, pp. 329-331.

Halfman, S.E., Lippmann, M.J., Zelwer, R. and Howard, J.H., 1984. Geologic interpretation of geothermal fluid movement in Cerro Prieto field, Baja California, México. American Association of Petroleum Geologists Bulletin, 68, 18–30.

1 Hanssen, R.F., 2001. Radar Interferometry: Data Interpretation and Error Analysis. Kluwer
2 Academic Publishers, Dordrecht, The Netherlands, 328 pp.
3 Herzig, C.T. and Jacobs, D.C., 1994. Cenozoic volcanism and two-stage extension in the Salton
4 trough, southern California and northern Baja California. Geology, 22(11), 991-994.
5 Hoffmann, J., Zebker, H., Galloway, D. and Amelung, F., 2001 Seasonal subsidence and
6 rebound in Las Vegas valley, Nevada, observed by synthetic aperture radar
7 interferometry. Water Resources Research, 37, 1551-1566.
8 Kampes, B., Hanssen, R. and Perski, Z., 2003. Radar interferometry with public domain tools,
9 FRINGE 2003, Frascati, Italy.
10 Lin, J. and Stein, R.S., 2004. Stress triggering in thrust and subduction earthquakes, and stress
11 interaction between the southern San Andreas and nearby thrust and strike-slip faults.
12 Journal of Geophysical Research, 109, B02303, doi:10.1029/2003JB002607.
13 Lippmann, M.J. and Bodvarsson, G.S., 1983. Numerical studies of the heat and mass transport in
14 the Cerro Prieto geothermal field, Mexico. Water Resources Research, 19(3), 753-767
15 Lippmann, M.J., Goldstein, N.E., Halfman, S.E. and Witherspoon, P.A., 1984. Exploration and
16 development of the Cerro Prieto geothermal field. Journal of Petroleum Technology,
17 36(9), 1579-1591.
18 Lippmann, M.J., Truesdell, A.H., Mañón, A.M. and Halfman, S.E., 1991. A review of the
19 hydrogeologic-geochemical model for Cerro Prieto. Geothermics, 20, 39-52.
20 Lippmann, M.J., Truesdell, A.H. and Frye, G., 1999. The Cerro Prieto and Salton Sea
21 geothermal fields – are they really alike? In Proceedings of twenty-fourth Workshop on
22 Geothermal Reservoir Engineering, Stanford University, Stanford, California, Report
23 SGP-TR-162, pp. 1-10.
24 Lippmann, M.J., Truesdell, A.H., Rodríguez, A.H. and Pérez, A., 2004. Response of Cerro Prieto
25 II and III to Exploitation. Geothermics, 33, 229-256.
26 Lira, H., 1996. Resultados del monitoreo de desplazamiento de la falla Cerro Prieto en 1996.
27 Informe Técnico RE 21/96, Comisión Federal de Electricidad, Residencia de Estudios,
28 México, 7 pp.
29 Lira, H., 1999a. Resultados del monitoreo de desplazamiento de la falla Cerro Prieto en 1998.
30 Informe Técnico RE 05/99, Comisión Federal de Electricidad, Residencia de Estudios,
31 México, 6 pp.

Lira, H., 1999b. Monitoreo de la Subsidencia en el Campo Geotérmico de Cerro Prieto, B.C., México. Geotermia, Revista Mexicana de Geoenergia, 15(1), 31-38.

Lira, H., 2005. Actualización del modelo geológico conceptual del yacimiento Geotérmico de Cerro Prieto. Geotermia, Revista Mexicana de Geoenergia, 18(1), 37-46.

Lira, H., 2006. Características del sismo del 23 de Mayo de 2006. Informe Técnico RE-023/2006, Comisión Federal de Electricidad, Residencia de Estudios, México.

Lira, H. and Arellano, J.F., 1997. Resultados de la nivelación de precisión realizada en 1997, en el campo geotérmico Cerro Prieto. Informe Técnico RE 07/97, Comisión Federal de Electricidad, Residencia de Estudios, México, 28 pp.

Lu, Z. and Danskin, W.R., 2001. InSAR analysis of natural recharge to define structure of a groundwater basin, San Bernardino, California. Geophysical Research Letters, 28, 2661-2664.

Massonnet, D. and Rabaute, T., 1993. Radar interferometry: limits and potential. IEEE Transactions on Geoscience and Remote Sensing, 31(2), 455-464.

Massonnet, D. and Feigl, K.L., 1998. Radar interferometry and its application to changes in the Earth's surface. Reviews of Geophysics, 36(4), 441–500.

Mogi, K., 1958. Relations between the eruptions of various volcanoes and the deformation of the ground surface around them. Bulletin of Earthquake Research Institute of University of Tokyo 36, 99 - 134.

Mossop, A. and Segall, P., 1997. Subsidence at the Geysers geothermal field, N. California from a comparison of GPS and leveling surveys. Geophysical Research Letters, 24(14), 1839–1842.

Ocampo Diaz; J. and De León, J., 2003, Efects of cold water recharge on downhole temperature wells of Cerro Prieto Uno area in Cerro Prieto Field Mexico. In Proceedings of Twenty-Eight Workshop on Geothermal Reservoir Engineering, Stanford University, Stanford, CA, SGP-TR-17.3

Okada, Y., 1992. Internal deformation due to shear and tensile faults in a half-space. Bulletin of the Seismological Society of America, 82, 1018-1040.

Potok, A.J., 1991. A Study of the Relationship between Subsidence and Flooding, the Fourth International Symposium on Land Subsidence, Houston, TX, USA, pp. 389-395.

Rosen, P. A., Hensley, S., Joughin, I.R., Li, F.K., Madsen, S.N., Rodriguez, E. and Goldstein, R.M., 2000. Synthetic aperture radar interferometry. In Proceedings of the IEEE, 88, pp. 333-382.

Sarychikhina, O., 2003. Modelación de subsidencia en el campo geotérmico Cerro Prieto. M.Sc. Thesis, Centro de Investigación Científica y Educación Superior de Ensenada, Ensenada, B.C., Mexico, 101 pp.

Sarychikhina, O., Glowacka, E. and Mellors, R., 2007. Preliminary results of a surface deformation study, using differential InSAR technique at the Cerro Prieto Geothermal Field, BC, Mexico. Geothermal Resources Council Transactions, 31, 581-584.

Sarychikhina, O., Glowacka, E., Mellors, R., Vázquez, R., Munguía, L. and Guzmán, M., 2009. Surface Displacement and Groundwater Level Changes Associated with the 24 May 2006 Mw 5.4 Morelia Fault Earthquake, Mexicali Valley, Baja California, Mexico. Bulletin of the Seismological Society of America, 99(4), 2180-2189.

Sarychikhina, O., 2010. The spatial and temporal distribution of the ground deformations in the Mexicali Valley in the context of tectonic, anthropogenic and seismic processes. Ph. D. Thesis, Centro de Investigación Científica y Educación Superior de Ensenada, Ensenada, B.C., Mexico, 135 pp.

Scharroo, R. and Visser, P., 1998. Precise orbit determination and gravity field improvement for the ERS satellites. Journal of Geophysical Research, 103(C4), 8113-8127

Schumann, H.H., Cripe, L.S. and Laney, R.L., 1986. Land subsidence and earth fissures caused by groundwater depletion in southern AZ, USA. In: Johnson, A.I., Carbognin, L. and Umbertini, L. (Eds.), the Third International Symposium on Land Subsidence. International Association of Hydrological Sciences (lAHS) Press and UNESCO, Venice, Italy, pp. 841-852.

Segall, P., 1989. Earthquakes triggered by fluid extraction. Geology, 17(10), 942.

Sheng, Z. and Helm, D.C., 1998. Multiple steps of earth fissuring caused by ground-water withdrawal. In: Borchers, J.W. (Ed.), Tectonic controls of geomorphic processes in land subsidence area. Land subsidence. Star Publishing Company, pp. 149–154.

Strozzi, T., Wegmüller, U., Tosi, L., Bitelli, G. and Spreckels, V., 2001. Land subsidence monitoring with differential SAR interferometry. Photogrammetric Engineering and Remote Sensing, 67(11), 1261-1270.

Suárez-Vidal, F., Munguía-Orozco, L., González-Escobar, M., González-García, J. and Glowacka, E., 2007. Surface rupture of the Morelia fault near the Cerro Prieto Geothermal Field, Mexicali, Baja California, Mexico, during the Mw 5.4 earthquake of 24 May 2006. Seismological Research Letters, 78(3), 394-399.

Suárez-Vidal, F., Mendoza-Borunda, R., Nafarrete-Zamarripa, L., Rámirez, J. and Glowacka, E., 2008. Shape and dimensions of the Cerro Prieto pull-apart basin, Mexicali, Baja California, México, based on the regional seismic record and surface structures. International Geology Review, 50(7), 636-649.

Toda, S., Stein, R. S., Richards-Dinger, K. and Bozkurt, S., 2005. Forecasting the evolution of seismicity in southern California: Animations built on earthquake stress transfer. Journal of Geophysical Research, B05S16, doi:10.1029/2004JB003415.

Truesdell, A., Lippman, M., Gutierrez Puente, H. and De Leon-Vivar, J., 1998. The importance of natural fluid recharge to the sustainability of the Cerro Prieto resource. Geothermal Resources Council Transactions, 22, 529-536.

Vasco, D. W., Wicks, C., Karasaki, K. and Marques, O., 2002. Geodetic imaging: reservoir monitoring using satellite interferometry. Geophysical Journal International, 149(3), 555-571.

Velasco, J., 1963. Levantamiento Gravimétrico, Zona Geotérmica de Mexicali, Baja California, Consejo de Recursos Naturales no Renovables.

Walsh, J.B., 2002. Subsidence above a planar reservoir. Journal of Geophysical Research, 107(B9), ETG 6-1.

Wang, G.Y., You, G., Shi, B., Yu, J., Li, H.Y. and Zong, K.H., 2009. Earth fissures triggered by groundwater withdrawal and coupled by geological structures in Jiangsu Province, China. Environmental Geology, 57, 1047-1054.

Watson, K.M., Bock, Y. and Sandwell, D.T., 2002. Satellite interferometric observations of displacements associated with seasonal groundwater in the Los Angeles basin. Journal of Geophysical Research, 107(B4), 2074, doi:10.1029/ 2001JB000470.

Wyman, R.M., 1983. Potential Modeling of Gravity and Leveling Data over Cerro Prieto Geothermal Field. M.Sc. Thesis, California State University, Long Beach, CA, USA, 79 pp.

Yang, X. and Davis, P.M., 1986. Deformation due to a rectangular tensional crack in an elastic half-space. Bulletin of the Seismological Society of America 76(3), 865-881.

Yong, R.N., Nutalaya, P., Mohamed, A.M.O. and Xu, D.M., 1991. Land subsidence and flooding in Bangkok, the Fourth International Symposium on Land Subsidence, Houston, TX, USA, pp. 407-416.

This work performed under the auspices of the U.S. Department of Energy by Lawrence Livermore National Laboratory under Contract DE-AC52-07NA27344.

Figure Captions:

Figure 1: Regional map of northern Baja California, Mexico and southern California, USA. Shuttle Radar Topography Mission Digital Elevation Model is used as background. Large white rectangles indicate the spatial coverage of ENVISAT ASAR images. D indicates descending track, and A indicates ascending track. White arrows indicate the radar look direction of the corresponding pass. The smaller white rectangle represents the study area. Smallest white filled rectangle represents the Cerro Prieto Geothermal Field. The principal tectonic faults and structures are also indicated: ABF = Agua Blanca Fault, BB = Brawley Basin, CDD = Cañada David Detachment, CPB = Cerro Prieto Basin, CPFZ = Cerro Prieto Fault Zone, EF = Elsinore Fault, IF = Imperial Fault, LSF = Laguna Salada Fault, SJF = Sierra Juarez Fault, SJFZ = San Jacinto Fault Zone, SMF = San Miguel Fault. Modified from Suárez-Vidal *et al.* (2008).

Figure 2: (a) SW-NE schematic geological section across Cerro Prieto pull-apart basin along the line indicated in Figure 2b (modified from Lira, 2005). The cracks of the best-fit model are superimposed. (b) Detailed plan of the study area with principal roads, villages and features, as Cerro Prieto volcano and evaporation pond (solid black line). Black dotted line frames the limits of the CPGF. A gray polygon indicates extraction area before year 2000; a yellow rectangle indicates the extraction area of CPIV which started the operation since 2000. Black squares mark the location of reference benchmarks. Solid red lines are well-known surface traces of tectonic faults. CPF=Cerro Prieto Fault, GF=Guerrero Fault, IF=Imperial Fault, MF=Morelia Fault, SF=Saltillo fault. SF and GF form a structure known as the Saltillo-Guerrero Graben (S-GG). Dotted red lines are proposed surface fault traces based on mapped fissure zones (brown squares) from González *et al.* (1998), Glowacka *et al.* (2006, 2010a), Lira (2006) and Suárez-Vidal *et al.* (2007, 2008), and wells data (as the case of HF=H fault, and LF=L fault) from Lippmann *et al.* (1984). SF' is continuation of Saltillo fault as proposed by Suárez-Vidal *et al.* (2008). HF_{β} is H fault on the intersection with the top of β_1 and β_2 reservoirs (solid rose lines). Modified from Glowacka *et al.* (2010a).

Figure 3: Perpendicular baseline information with respect to the first acquisition of each dataset. A and D indicate ascending and descending tracks, respectively. Label in each point represents

the orbit of the image. Black lines represent interferometric pairs presented in this article. X axis minor ticks mark 35 days period which is the revisiting period of ENVISAT satellite.

Figure 4: Geocoded differential interferograms. Areas of low coherence (<0.1) are masked. D indicates descending track. Black dotted line frames the limits of the CPGF. Faults notation is as in Figure 2b.

Figure 5: Geocoded LOS displacement maps used for stacking. Areas of low coherence (<0.1) are masked. Magenta dotted triangle marks the limits of the area considered stable and used in the estimation of the error of LOS displacement for the single interferogram. Black dotted line frames the limits of the CPGF. Black square shows location of the reference benchmark "10037". Faults notation is as in Figure 2b.

Figure 6: a. Geocoded map of LOS displacement rate (cm/yr) for December 2004-December 2005 period obtained using the stacking technique. b and c. Best-fit model predicted LOS displacements. d. Residuals between observed (a) and predicted (b) LOS displacements. Areas of low coherence (<0.1) are masked in a, b, and d. Black square shows location of the reference benchmark "10037". Black dotted line frames the limits of the CPGF. Black lines correspond to the profiles A-A', B-B' and C-C' illustrated in Figure 7. Brown rectangles in b and d show the tensional rectangular cracks of the best-fit model (Table 4). Faults notation is as in Figure 2b.

Figure 7: Comparison between DInSAR data (black circles), derived from interferograms stacking, and model prediction (thick discontinuous line) along the profiles which location is shown in Figure 6a. Black circles are DInSAR data. Error bars indicate expected LOS displacement rate estimation error of DInSAR data which is ±1.5 cm/yr. Positive LOS displacement values indicate ground subsidence. Thin lines, continuous and discontinuous, are faults which cross the profiles. Faults notation is as in Figure 2b.

Figure 8: Contour maps of LOS displacement velocity (cm/yr) obtained using data from leveling surveys 1994-1997 (a) and 1997-2006 (b), and DInSAR stacking 2004-2005 (c & d).The contours were obtained by interpolation of the data using the Kriging algorithm. Contouring of DInSAR stacking data was performed using the value of all pixels with coherence >0.1 (c) and only these in location of the 1994-1997 leveling benchmarks (d). Black dotted line frames the

limits of the CPGF. Black square shows location of the reference benchmark "10037". Gray squares are benchmarks used for interpolation and contouring. Faults notation is as in Figure 2b.

Figure 9: Vertical displacement from leveling surveys 1994-1997 (a) and predicted by the best-fit model (b). (c) Residuals between observed (a) and predicted (b) vertical displacements. Black square shows location of the reference benchmark "10037". Gray squares are leveling benchmarks. Black dotted line frames the limits of the CPGF. Brown rectangles in b and c show the tensional rectangular cracks of the best-fit model. Faults notation is as in Figure 2b.

Figure 10: Evolution of the net extraction of geothermal fluid (extraction-injection) in CPGF from 1990 to 2005 (modified from page 27, CFE (2006)).

Figure 11: The spatial localization of unknown but expected faults or structural limits (F1, F2 and F3), based on observed subsidence pattern and/or results of modeling (blue rectangles). DInSAR stacking data (2004-2005) with masked areas of low coherence (<0.1) are shown as background. Black square shows location of the reference benchmark "10037". Black dotted line frames the limits of the CPGF. Brown squares indicate the location of fissure/fault zones mapped by González *et al*. (1998), Glowacka *et al.* (2006, 2010a), Lira (2006) and Suárez-Vidal *et al*. (2007, 2008). Faults notation is as in Figure 2b. Brown rectangles show the tensional rectangular cracks of the best-fit model.

Table 1. List of ENVISAT ASAR images used for this study. A and D indicate ascending and descending tracks, respectively.

DATE	ORBIT	TRACK	FRAME	PASS
2003/10/26	8655	84	2961	D
2004/05/23	11661	84	2961	D
2004/09/05	13164	84	2961	D
2004/10/10	13665	84	2961	D
2004/12/19	14667	84	2961	D
2005/01/23	15168	84	2961	D
2005/02/27	15669	84	2961	D
2005/04/03	16170	84	2961	D
2005/05/08	16671	84	2961	D
2005/06/12	17172	84	2961	D
2005/07/17	17673	84	2961	D
2005/08/21	18174	84	2961	D
2005/09/25	18675	84	2961	D
2005/10/30	19176	84	2961	D
2005/12/04	19677	84	2961	D
2006/02/12	20679	84	2961	D
2006/03/19	21180	84	2961	D
2003/12/16	9378	306	639	A
2004/02/24	10380	306	639	A
2004/05/04	11382	306	639	A
2006/04/04	21402	306	639	A
2006/05/09	21903	306	639	A

Table 2. Interferometric parameters of the DInSAR pairs presented in this paper. A and D indicate ascending and descending tracks, respectively. Gray shading indicates interferometric pairs used for stacking. [a] Pairs as presented in Figure 4.

PAIRS[a]	MASTER	SLAVE	TRACK_FRAME	$B_{\perp}$ (m)	B_{temp} (days)
a	2003/12/16	2004/02/24	306_369 (A)	-157	70
b	2003/10/26	2004/10/10	84_2961 (D)	-147	350
c	2004/12/19	2005/02/27	84_2961 (D)	112	70
d	2005/02/27	2005/06/12	84_2961 (D)	-53	105
e	2005/06/12	2005/09/25	84_2961 (D)	206	105
f	2005/09/25	2005/12/04	84_2961 (D)	-260	70

Table 3. Estimated uncertainty in the LOS displacement (cm) for single interferogram. The estimation was performed for each interferogram used in the stacking.

Master	*Slave*	*Uncertainty in the LOS displacement (cm)*
2004/12/19	2005/02/27	0.6
2005/02/27	2005/06/12	1.2
2005/06/12	2005/09/25	0.5
2005/09/25	2005/12/04	0.6
	Average:	***0.7***

Table 4. Models cracks parameters. 94-97 is the model which fits the leveling 1994-1997 data. 2005 is the model which fits the DInSAR data. Crack closing (p) is positive.

Crack	*Model Cracks Parameters*								
	x (m)	**y (m)**	**z (m)**	**L (m)**	**W (m)**	**Azm. (°)**	**Ang. (°)**	**p (m)**	
								94-97	**2005**
α_1	664224	3586226	1028	4142	3151	136	1	0.075	0.015
α_2	667518	3582923	1448	4569	3151	136	1	0.035	0.035
β_1	667739	3587407	2060	1435	4014	138.5	4	0.12	0.12
β_2	669054	3585919	2460	1836	4014	138.5	4	0.12	0.15
sr	673482	3589177	2800	3796	4923	134	7	0.115	0.23
LR1	669372	3587781	862	9474	12778	136	1	0.04	0.04
LR2	671460	3581382	810	2624	6876	136	1	0.04	0.04

Table 5. Volume change caused by cracks closing.

Crack	*Volume change (m^3/yr)*	
	1994-1997	**2005**
α_1	9.79E+05	1.96E+05
α_2	5.04E+05	5.04E+05
β_1	6.91E+05	6.91E+05
β_2	8.84E+05	1.11E+06
sr	2.15E+06	4.30E+06
LR1	4.84E+06	4.84E+06
LR2	7.22E+05	7.22E+05
Total	1.08E+07	1.24E+07

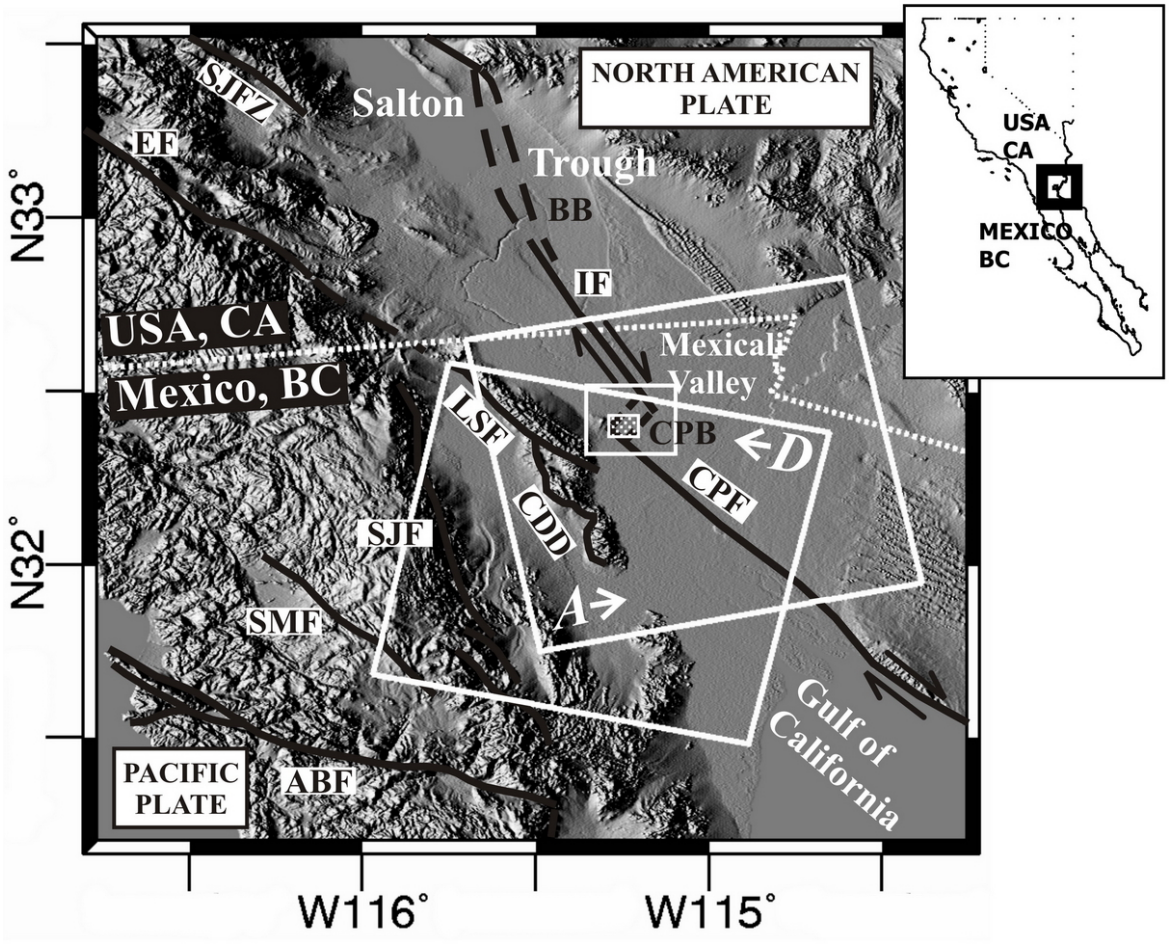
NORTH AMERICAN PLATE
SJFZ
EF
Salton
Trough
BB
IF
USA, CA
Mexico, BC
Mexicali Valley
CPB
D
CPF
LSF
CDD
SJF
A
SMF
PACIFIC PLATE
ABF
Gulf of California
N33°
N32°
W116°
W115°
USA
CA
MEXICO
BC

Figure 1.

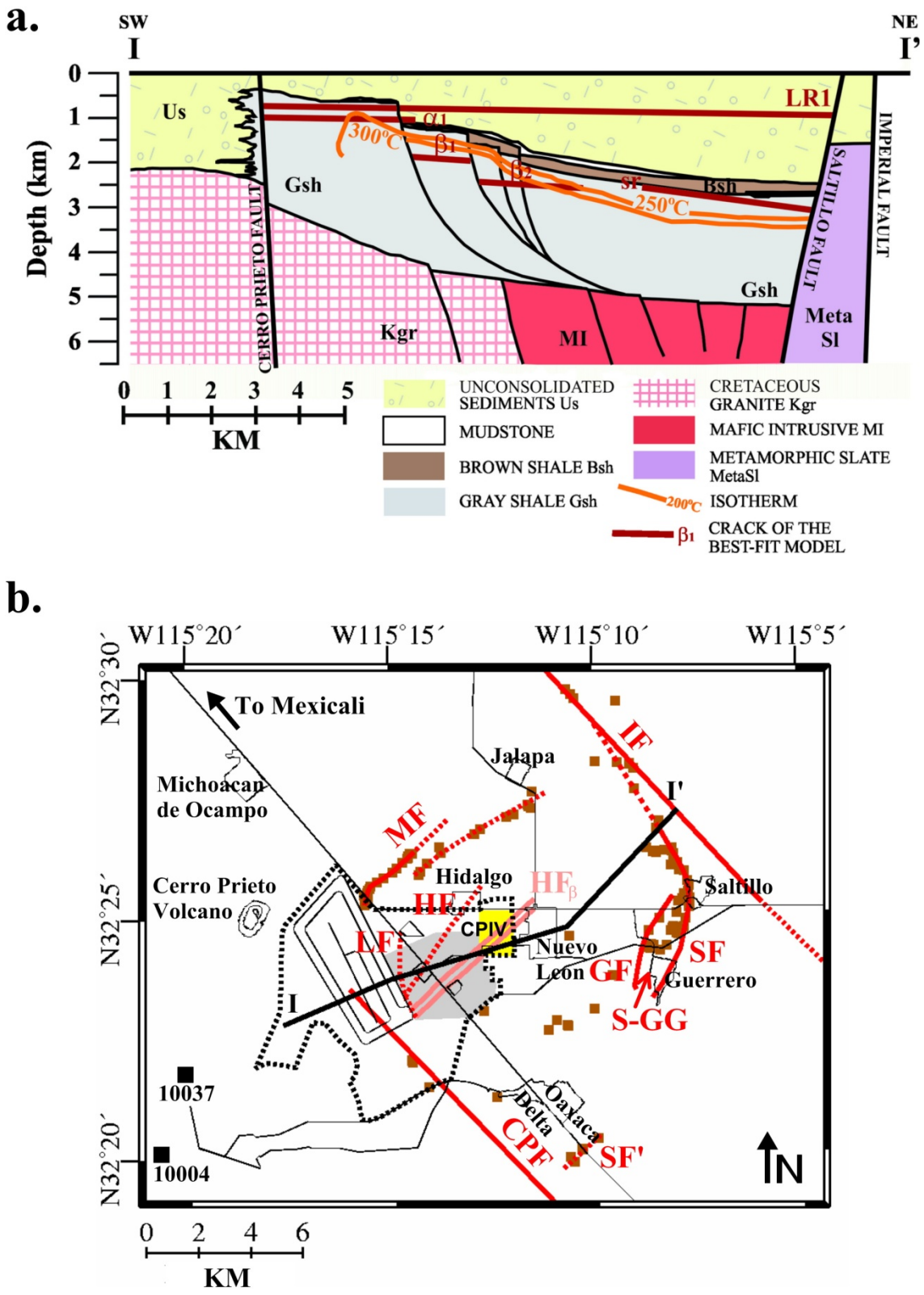
a.
SW
I
NE
I'
Depth (km)
0
1
2
3
4
5
6
Us
LR1
300°C
β1
β2
SF
Bsh
250°C
Gsh
CERRO PRIETO FAULT
IMPERIAL FAULT
SALTILLO FAULT
Kgr
MI
Meta
Sl
0 1 2 3 4 5
KM
UNCONSOLIDATED SEDIMENTS Us
MUDSTONE
BROWN SHALE Bsh
GRAY SHALE Gsh
CRETACEOUS GRANITE Kgr
MAFIC INTRUSIVE MI
METAMORPHIC SLATE MetaSl
200°C ISOTHERM
β1 CRACK OF THE BEST-FIT MODEL
b.
W115°20′
W115°15′
W115°10′
W115°5′
N32°30′
N32°25′
N32°20′
To Mexicali
Michoacan de Ocampo
Jalapa
IF
I'
MF
Hidalgo
HFβ
HF
Cerro Prieto Volcano
Saltillo
CPIV
LF
Nuevo Leon
GF
SF
Guerrero
I
S-GG
10037
10004
Delta
Oaxaca
CPF
SF'
N
0 2 4 6
KM

Figure 2.

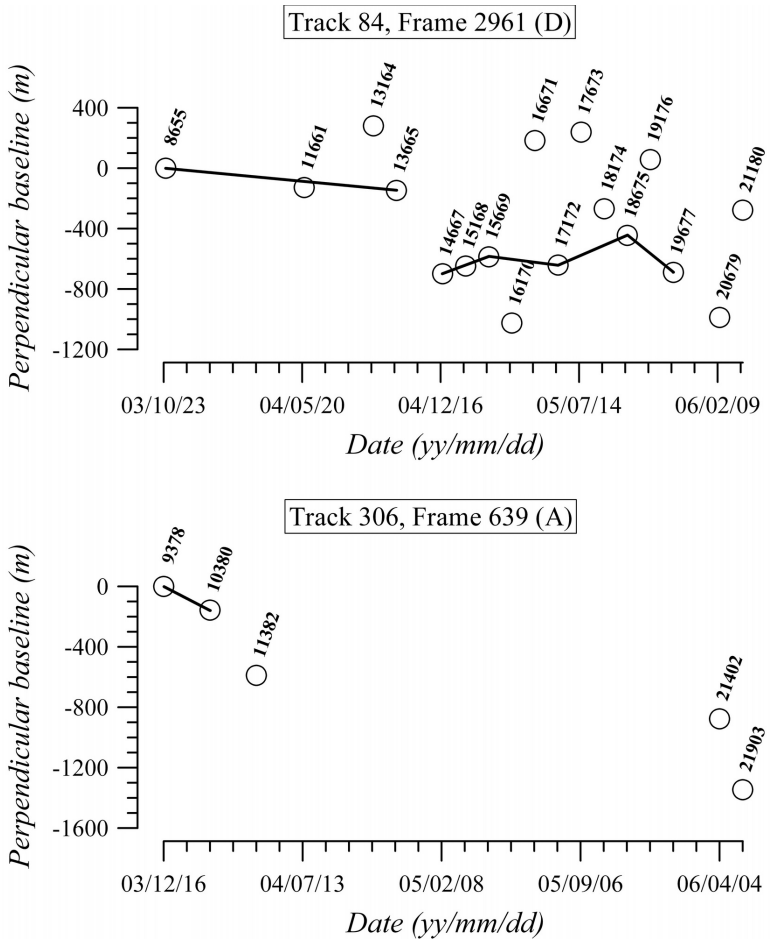
Track 84, Frame 2961 (D)
Perpendicular baseline (m)
400
0
-400
-800
-1200
8655
11661
13164
13665
14667
15168
15669
16170
16671
17172
17673
18174
18675
19176
19677
20679
21180
03/10/23
04/05/20
04/12/16
05/07/14
06/02/09
Date (yy/mm/dd)
Track 306, Frame 639 (A)
Perpendicular baseline (m)
0
-400
-800
-1200
-1600
9378
10380
11382
21402
21903
03/12/16
04/07/13
05/02/08
05/09/06
06/04/04
Date (yy/mm/dd)

Figure 3.

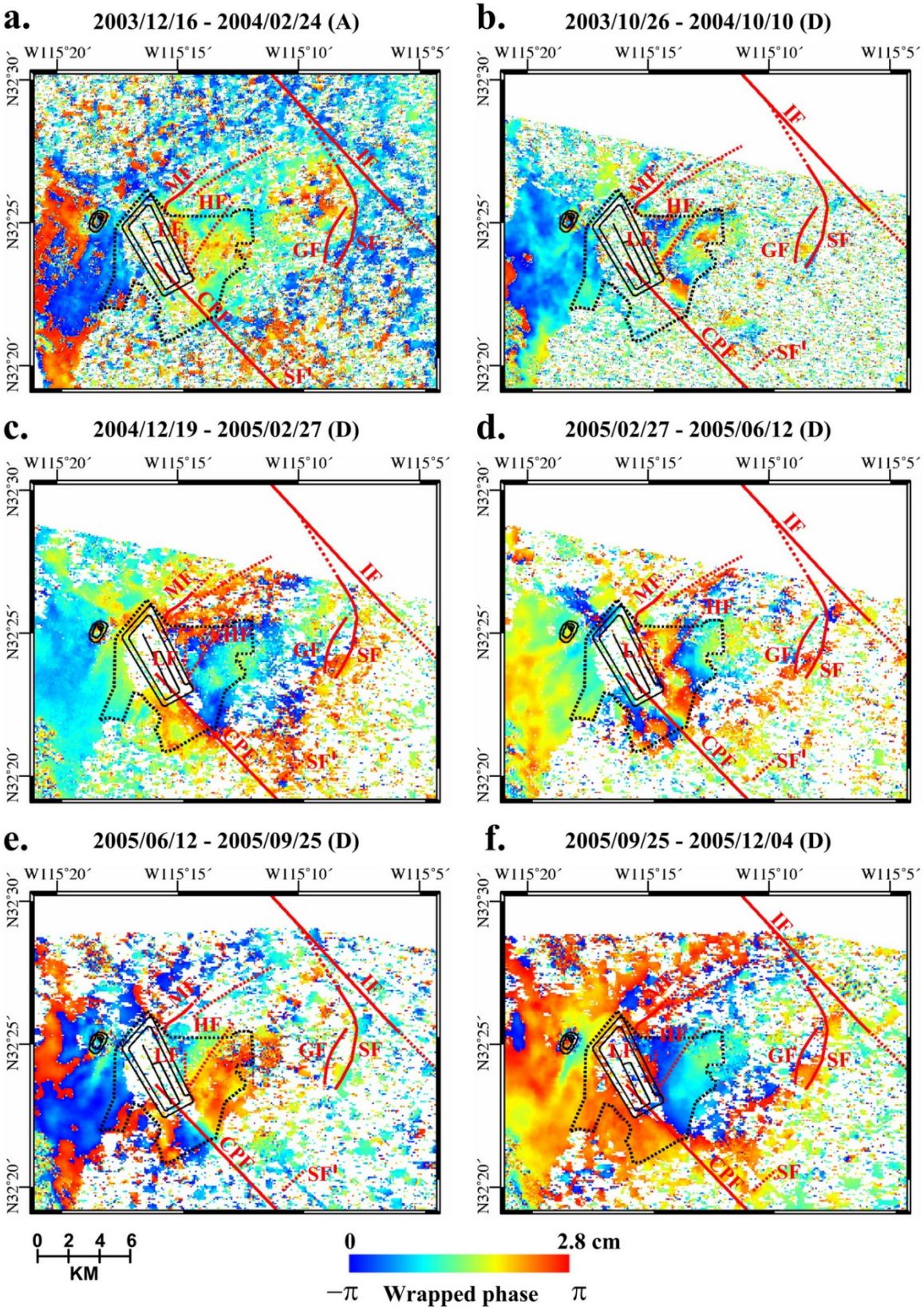
a.
2003/12/16 - 2004/02/24 (A)
b.
2003/10/26 - 2004/10/10 (D)
c.
2004/12/19 - 2005/02/27 (D)
d.
2005/02/27 - 2005/06/12 (D)
e.
2005/06/12 - 2005/09/25 (D)
f.
2005/09/25 - 2005/12/04 (D)
W115°20′
W115°15′
W115°10′
W115°5′
N32°30′
N32°25′
N32°20′
MF
HF
LF
IF
GF
SF
CPF
SF'
0 2 4 6
KM
0
2.8 cm
−π
Wrapped phase
π

Figure 4.

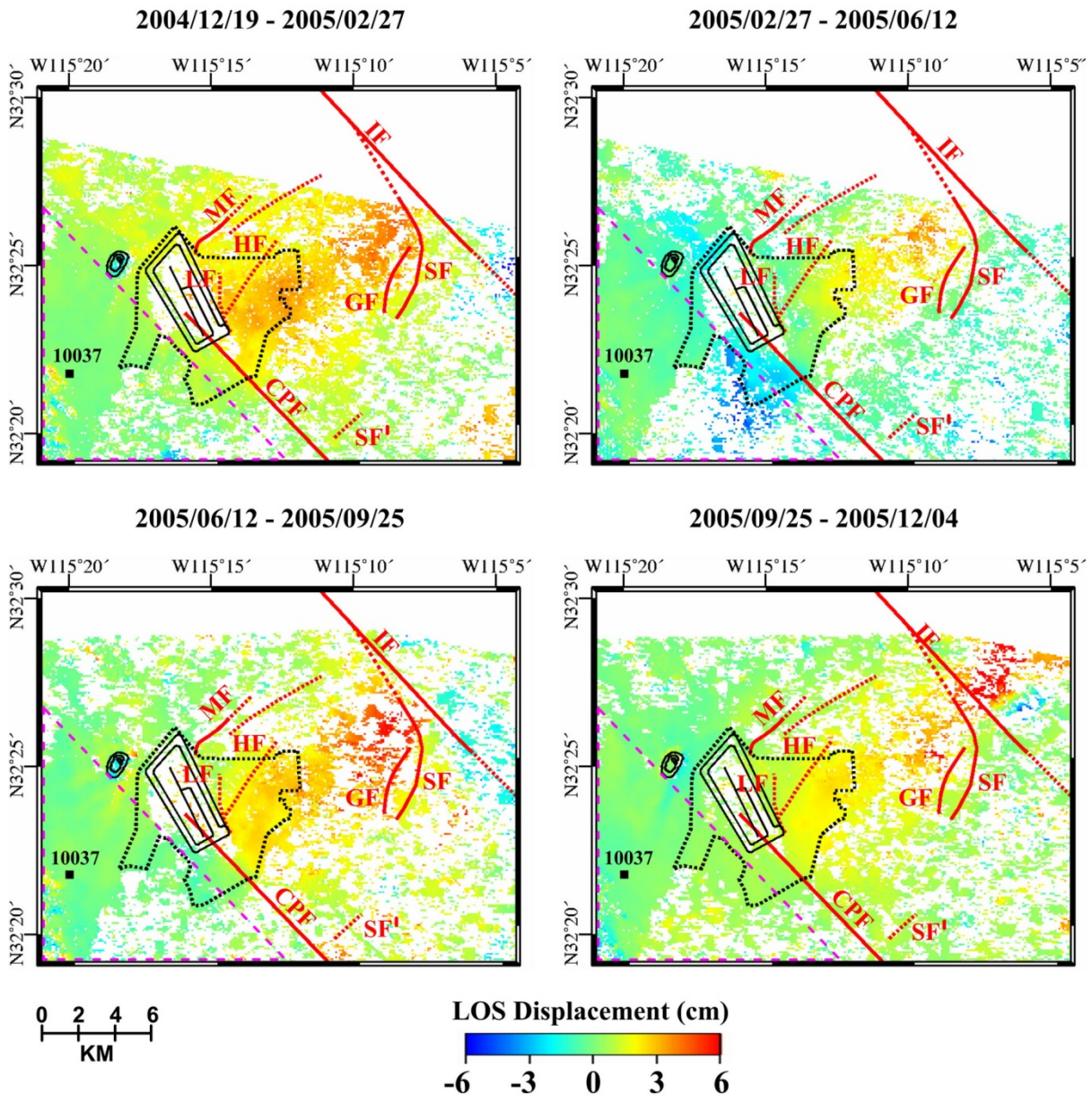
2004/12/19 - 2005/02/27
2005/02/27 - 2005/06/12
2005/06/12 - 2005/09/25
2005/09/25 - 2005/12/04
W115°20′
W115°15′
W115°10′
W115°5′
N32°30′
N32°25′
N32°20′
IF
MF
HF
LF
GF
SF
SF'
CPF
10037
0 2 4 6
KM
LOS Displacement (cm)
-6 -3 0 3 6

Figure 5.

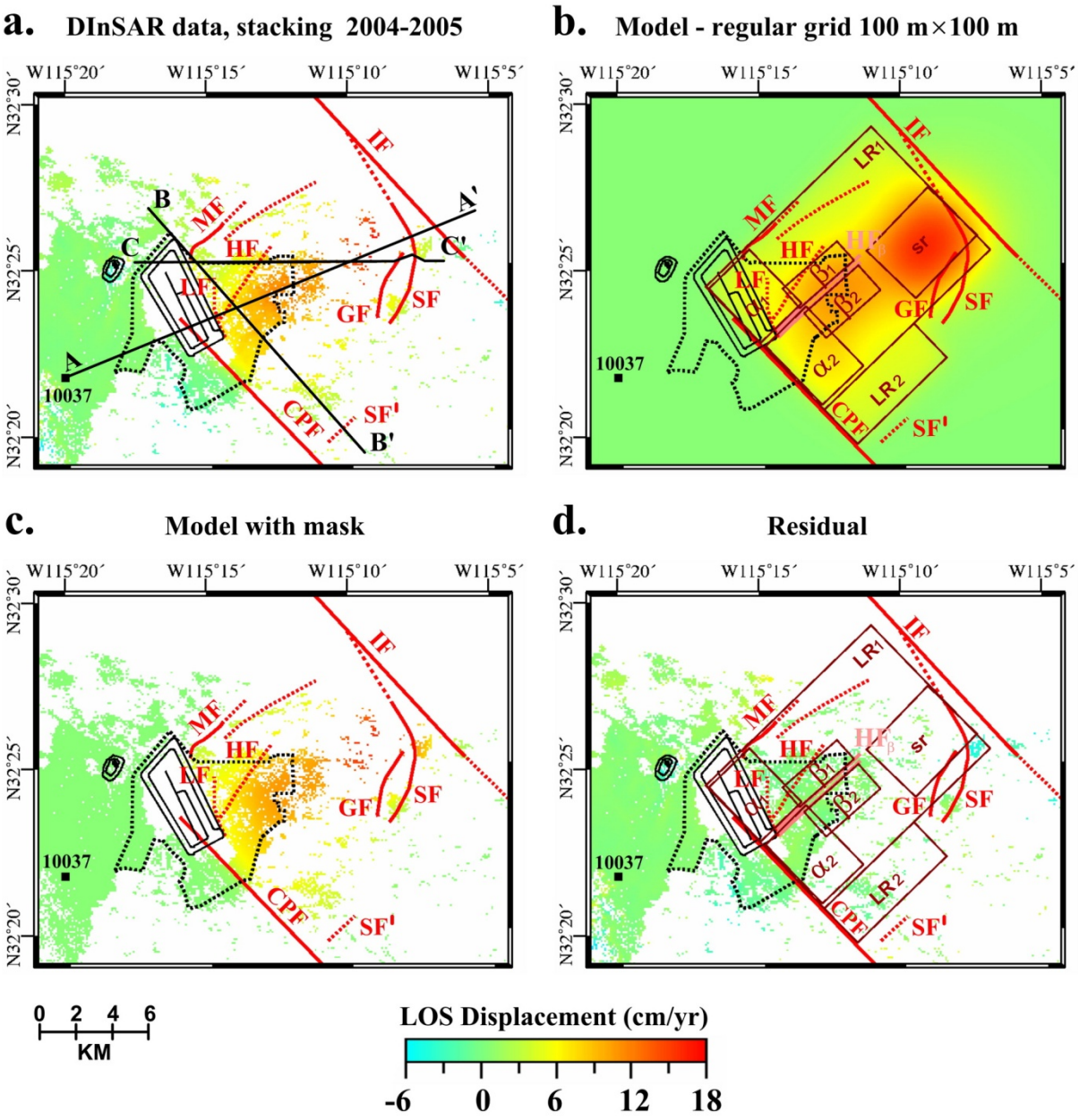
a. DInSAR data, stacking 2004-2005
b. Model - regular grid 100 m×100 m
c. Model with mask
d. Residual
W115°20′
W115°15′
W115°10′
W115°5′
N32°30′
N32°25′
N32°20′
IF
MF
HF
LF
GF
SF
SF'
CPF
LR1
LR2
A
A'
B
B'
C
C'
10037
0 2 4 6
KM
LOS Displacement (cm/yr)
-6 0 6 12 18

Figure 6.

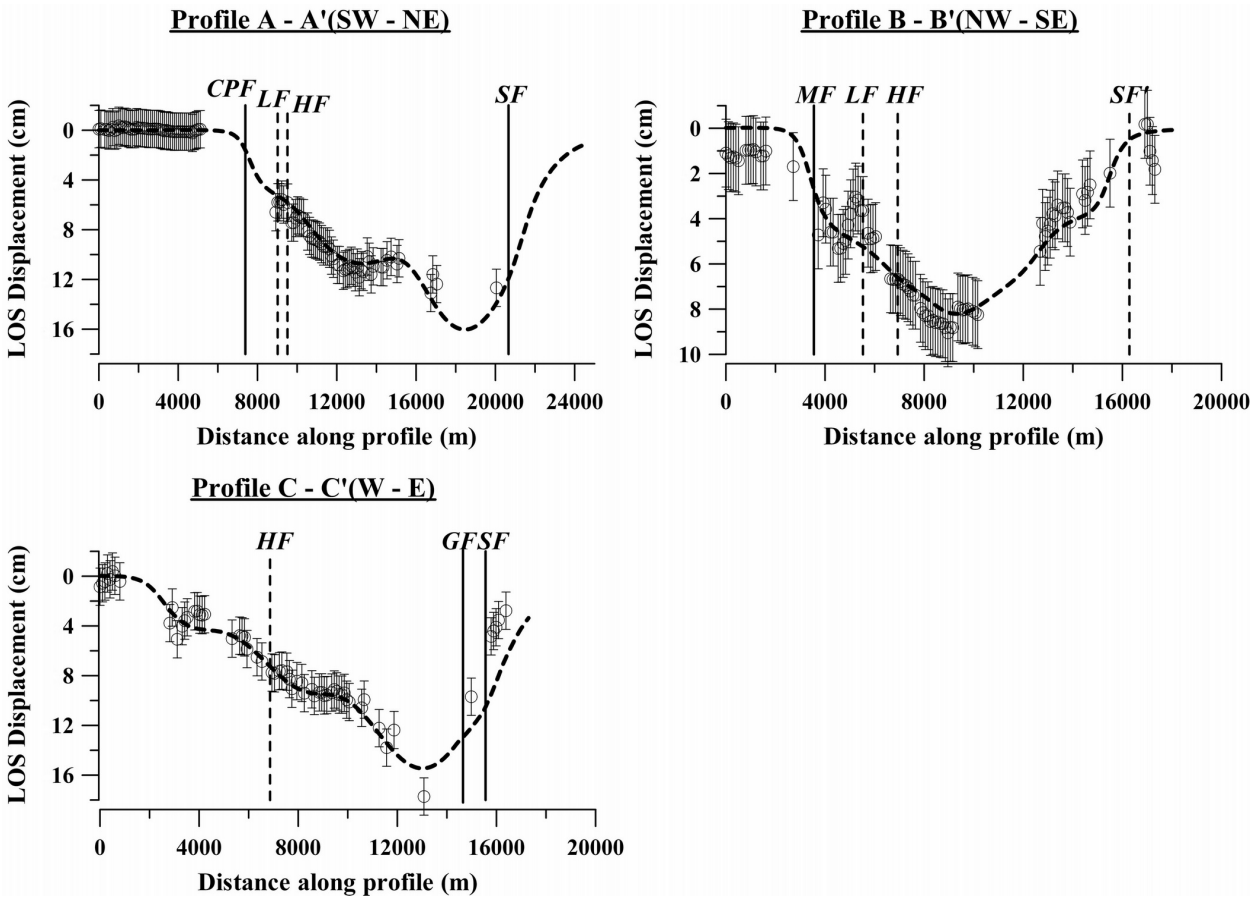
Profile A - A'(SW - NE)
CPF
LF
HF
SF
LOS Displacement (cm)
0
4
8
12
16
0
4000
8000
12000
16000
20000
24000
Distance along profile (m)
Profile B - B'(NW - SE)
MF
LF
HF
SF
LOS Displacement (cm)
0
2
4
6
8
10
0
4000
8000
12000
16000
20000
Distance along profile (m)
Profile C - C'(W - E)
HF
GF
SF
LOS Displacement (cm)
0
4
8
12
16
0
4000
8000
12000
16000
20000
Distance along profile (m)

Figure 7.

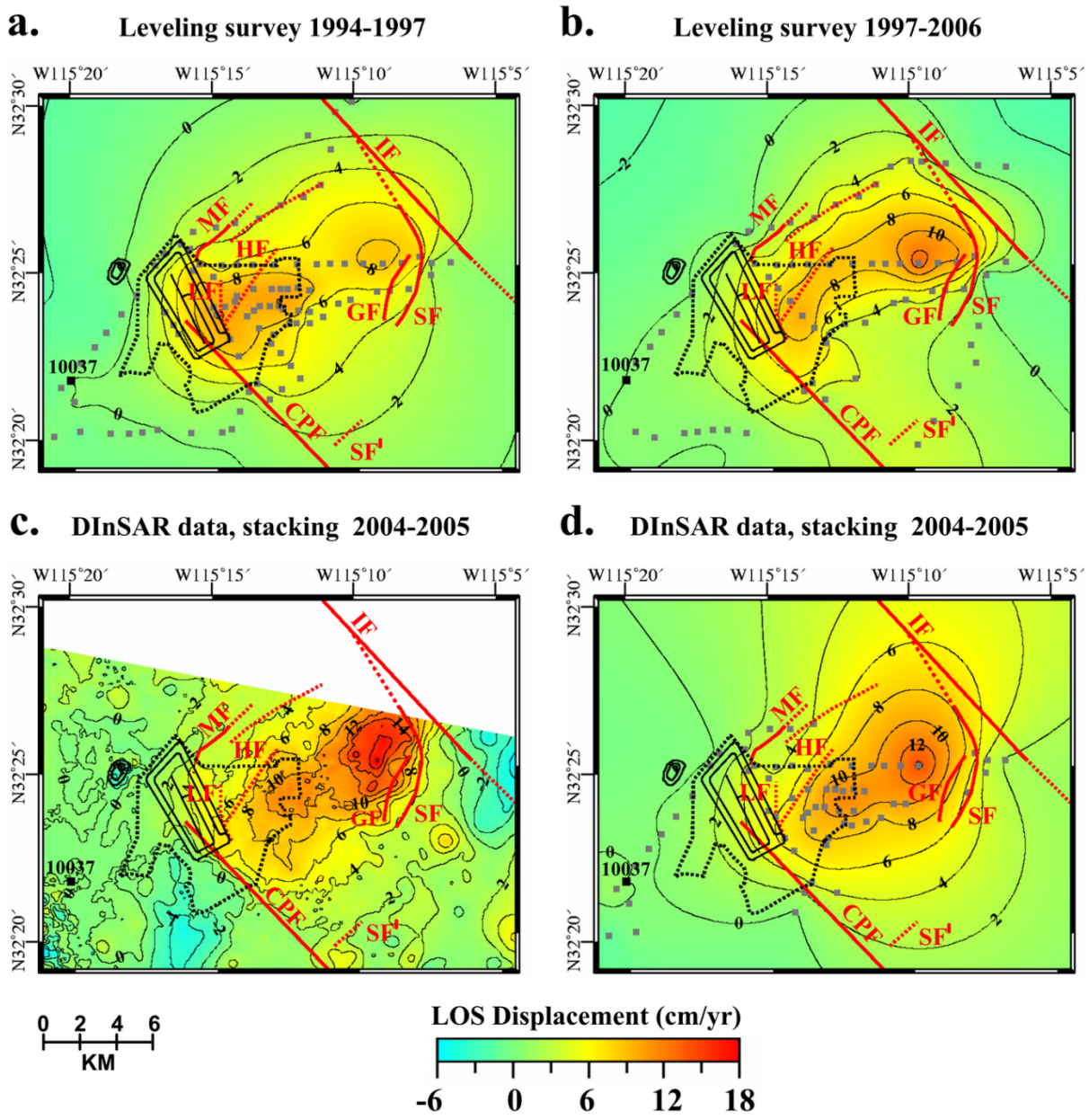
a. Leveling survey 1994-1997
b. Leveling survey 1997-2006
c. DInSAR data, stacking 2004-2005
d. DInSAR data, stacking 2004-2005
W115°20′
W115°15′
W115°10′
W115°5′
N32°30′
N32°25′
N32°20′
IF
MF
HF
LF
GF
SF
CPF
SF'
10037
0 2 4 6
KM
LOS Displacement (cm/yr)
-6 0 6 12 18

Figure 8.

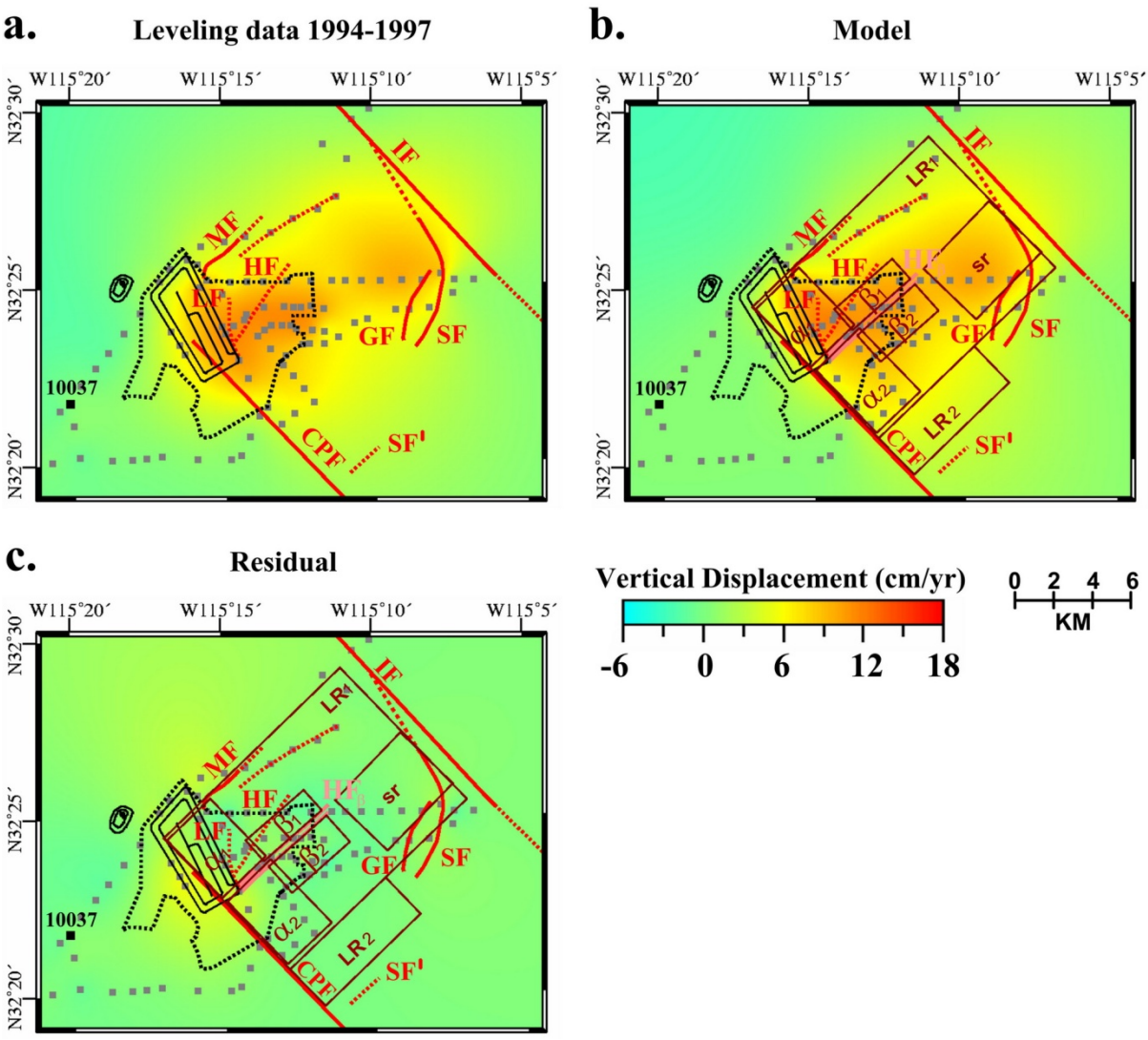
a.
Leveling data 1994-1997
b.
Model
c.
Residual
W115°20′
W115°15′
W115°10′
W115°5′
N32°30′
N32°25′
N32°20′
IF
MF
HF
LF
GF
SF
SF'
CPF
LR
LR1
LR2
10037
Vertical Displacement (cm/yr)
-6
0
6
12
18
0 2 4 6
KM

Figure 9.

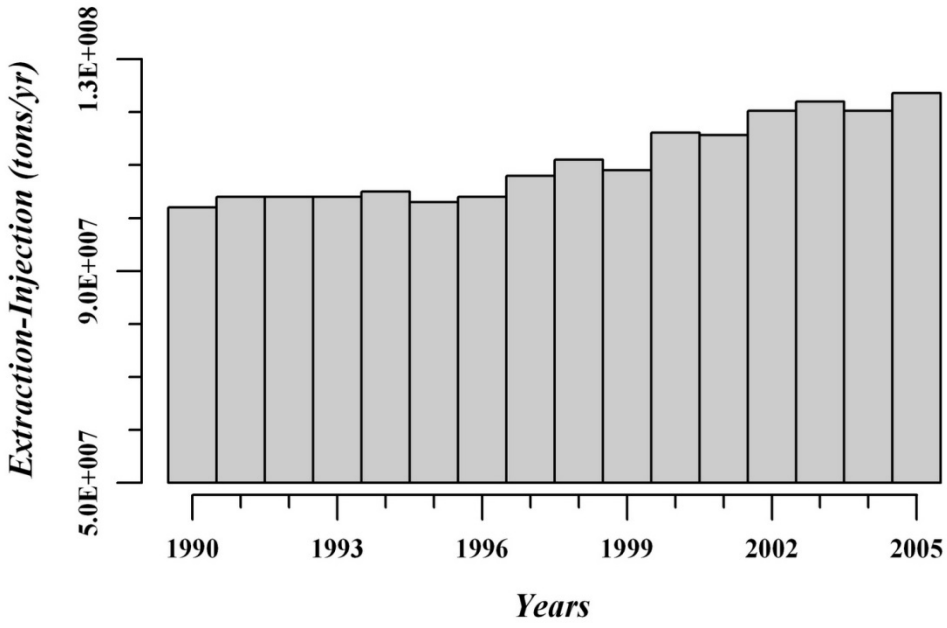

Figure 10.

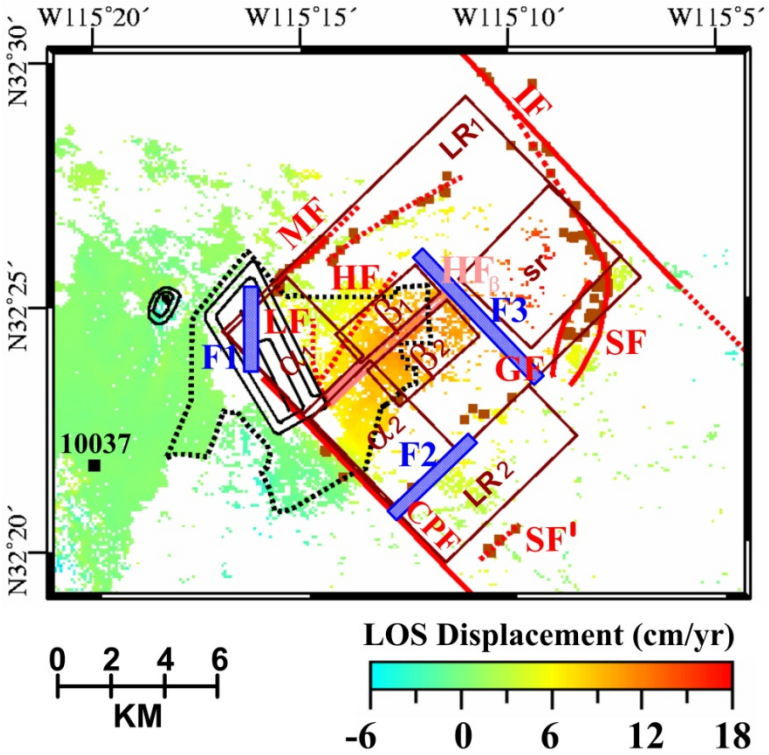

Figure 11.